



Research paper

Sawtooth patterns in flexural force curves of structural biological materials are not signatures of toughness enhancement: Part II

Wenqiang Fang, Sayaka Kochiyama, Haneesh Kesari *

Brown University, School of Engineering, 184 Hope Street, Providence, RI, USA

ARTICLE INFO

Keywords:

Structure–property relationship
 Experimental mechanics
 Stick–slip phenomenon
 Architected materials

ABSTRACT

Stiff biological materials (SBMs), such as nacre and bone, are composites that display remarkable toughness enhancements over their primary constituents, which are brittle minerals. These enhancements are thought to be a consequence of different mechanisms made possible by the SBMs' internal lamellar architecture. One such mechanism is the Cook–Gordon (crack-arrest-and-reinitiation) mechanism, whose operation manifests in flexural tests as a sawtooth pattern in the force–displacement curves. The curves from flexural tests carried out on marine sponge spicules, which also possess a lamellar architecture, also display a sawtooth-pattern, suggesting the presence of the Cook–Gordon mechanism. Intriguingly, the spicules were recently found not to display any significant toughness enhancement. To resolve this apparent contradiction, in the preceding paper (Kochiyama et al., 2021), we put forward the hypothesis that the sawtooth pattern was due to the spicules slipping at the tests' supports. In this paper, we present a model for the spicule's flexural tests in which we allow for the possibility for the specimen to slip at the test's supports. We model contact between the specimen and the test's supports using the Coulomb's friction law. By choosing experimentally reasonable values for the friction coefficient, we were able to get the model's predictions to match experimental measurements remarkably well. Additionally, on incorporating the spicules' surface roughness into the model, which we did by varying the friction coefficient along the spicule's length, its predictions can also be made to match the measured sawtooth patterns. We find that the sawtooth patterns in the model are due to slip type instabilities, which further reinforces the hypothesis put forward in our preceding paper.

1. Introduction

Stiff biological materials (SBMs), such as nacre and bone, are natural layered composites that are known for having remarkable fracture toughness that can be orders of magnitude higher than that of the brittle ceramics that dominates their composition (Jackson et al., 1988; Currey, 1977; Sarikaya, 1994; Menig et al., 2000; Koester et al., 2008; Wegst et al., 2015). The key to such enhancement in fracture toughness lies in their lamellar architectures, which are the intricate arrangements of ceramic and organic phases at the sub-micron scales (see Fig. 1(A) & (B)). One way in which the lamellar architecture contributes to the toughness enhancement is by supporting the operation of the Cook–Gordon (crack-arrest-and-reinitiation) mechanism (Cook et al., 1964). In this mechanism, when a crack initiates in and propagates through the ceramic phase, the organic phase, which separates one region of the ceramic phase from another, can effectively act as a “trap” and arrest the crack (Ming-Yuan and Hutchinson, 1989; Cook et al., 1964). In flexural tests, the operation of the Cook–Gordon mechanism reflects as a drop in the measured force as the crack advances, and

then as the end of that force drop as the crack gets arrested (Clegg et al., 1990). As such, when the Cook–Gordon mechanism operates in layered materials, the measured force–displacement curve can have the appearance of a sawtooth pattern (see Fig. 2(B)).

Monn et al. recently showed that the presence of lamellar architectures by itself does not necessarily guarantee the operation of the Cook–Gordon mechanism (Monn et al., 2020). They demonstrated this using the fiber-like glass skeletal elements, called spicules (see Fig. 1(C)), of the marine sponge *Euplectella aspergillum* (*Ea.*). The *Ea.* spicules also have a lamellar architecture that resembles those in nacre and bone. The architecture consists of alternating layers of glass and organic phase laid out in a concentric manner, as shown in Fig. 1(D). Monn et al. performed notched three-point bending tests on the spicules and directly measured their fracture toughness in terms of the initiation fracture toughness and the average crack growth resistance, and found that the fracture toughness enhancement in them was negligible (Monn et al., 2020). This implied that the Cook–Gordon mechanism either operated to a negligible level or was absent in the spicules.

* Corresponding author.

E-mail address: haneesh_kesari@brown.edu (H. Kesari).

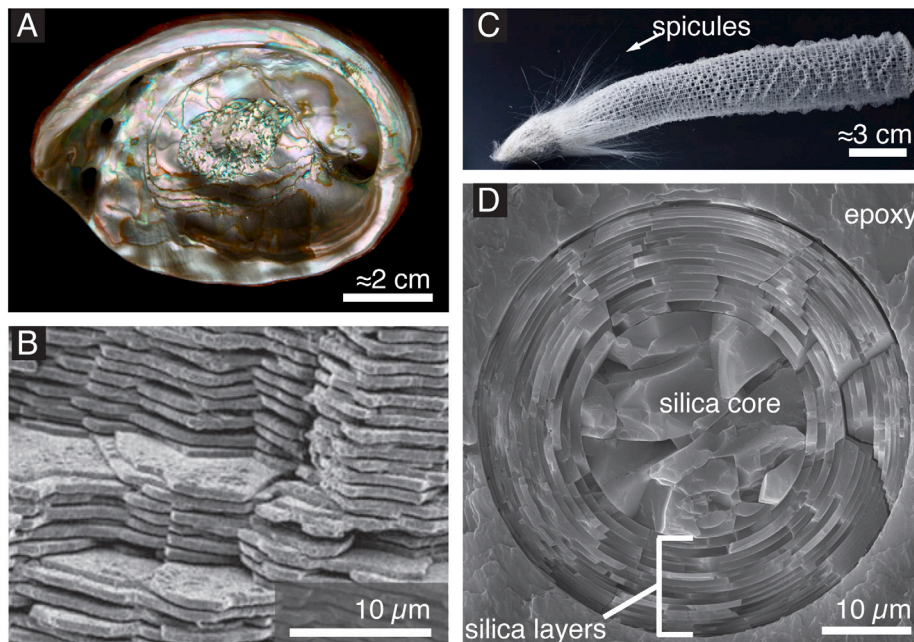


Fig. 1. Lamellar architectures in biological materials. (A) The shell of *Haliotis rufescens*—the red abalone (image courtesy of John Varner). (B) The nacre from *H. rufescens* consists of aragonite tablets assembled in a brick-and-mortar manner, where thin protein layers (not identifiable in the image) in-between the tablets function as the mortar (modified with permission from Rabeii et al. (2012); copyright 2012 the Royal Society of Chemistry). Owing to such arrangement, nacre demonstrates a 1000-fold increase in fracture toughness compared to that of the mineral aragonite. (C) The entire skeletal structure of a marine sponge *Euplectella aspergillum* is shown (modified from Monn et al. (2015); copyright 2015 National Academy of Sciences). The white arrow identifies the spicules, which are around 50 μm in diameter and can be several centimeters long. In some of our recent studies, we performed three-point bending tests on these spicules (Monn and Kesari, 2017; Monn et al., 2020). (D) A scanning electron microscope (SEM) image of a *E. aspergillum* spicule's cross section shows lamellar architecture consisting of a cylindrical silica core surrounded by concentric silica layers (modified from Monn et al. (2015); copyright 2015 National Academy of Sciences). Each of these concentric silica layers are separated from their adjacent layers or the silica core by a compliant organic layer whose thickness is roughly in the 5–10 nm range (not identifiable in the SEM image) (Weaver et al., 2007).

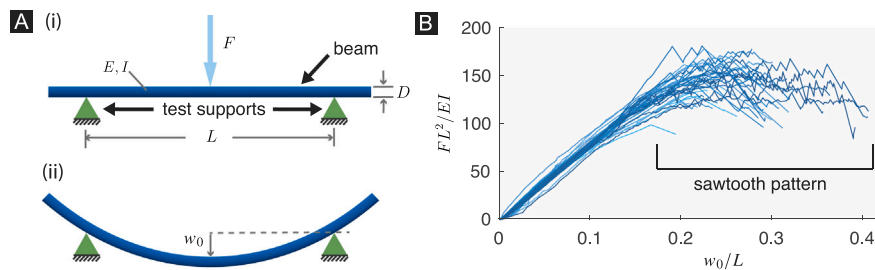


Fig. 2. (A)(i) Typical schematic of a three-point bending test in its reference configuration and (ii) the deformed beam with midpoint displacement w_0 under the action of some midpoint force F . The support span is L , and D , E , and $I = \pi D^4/64$ are the diameter, Young's modulus, and the bending moment of inertia of the beam, respectively. (B) Thirty eight scaled force-displacement curves from three-point bending tests carried out on *E. aspergillum* spicules and previously presented in Monn and Kesari (2017), Kochiyama et al. (2021). The spicules respond linearly until a certain point, then, in most cases, start displaying the sawtooth pattern.

However, the implication that the Cook–Gordon mechanism operates to an insignificant level during the failure of *Ea.* spicules in flexural tests appears to contradict the observations made in Monn and Kesari (Sarikaya et al., 2001; Levi et al., 1989; Monn and Kesari, 2017). To be specific, in Monn and Kesari (2017) Monn and Kesari carried out three-point bending tests on *Ea.* spicules. They observed sawtooth patterns in the force–displacement curves from their tests, in which the spicules were being loaded all the way until failure (see Fig. 2). As intimated previously, sawtooth-patterns in layered materials are usually a signature of the operation of the Cook–Gordon mechanism (Clegg et al., 1990). Therefore, if the Cook–Gordon mechanism is indeed irrelevant during the spicule's failure as argued in Monn et al. there must be alternative explanations for the appearance of the sawtooth patterns observed in the force–displacements curves of Monn and Kesari.

In Part I of the current paper (Kochiyama et al., 2021), we attempt to resolve the apparent contradiction by hypothesizing that the sawtooth patterns, at least in the case of *Ea.* spicules, are solely the consequence of the spicules slipping (see Fig. 3(B)) at the test's

supports, rather than of the operation of the Cook–Gordon mechanism. We summarize our arguments from Part I of this paper in the following few paragraphs.

In Kochiyama et al. (2021) we reported force–displacement measurements from three-point bending tests that were carried out on *Ea.* spicules in the simply-supported (SS) setup (see Fig. 2). Micrographs of the spicules were taken *in-situ* via a microscope during the tests. By conducting image analysis on those micrographs, it was demonstrated that in the tests in which the force–displacement curve displayed a sawtooth pattern, there were sudden jumps in the total length of the spicule section lying between the test's supports. This total length is shown marked as S in Fig. 3(B)(ii).2. The jumps appear, e.g., as the discontinuities in the green curve shown in Fig. 3(B)(iii). It was further shown that the jumps and the force-drop events (which appear, e.g., as the discontinuities in the blue curve in Fig. 3(B)(iii)) took place at the exact same time instances. These observations imply one of the following three scenarios: (i) the force-drop events are solely due to the layer-fracture events associated with the Cook–Gordon mechanism, (ii)

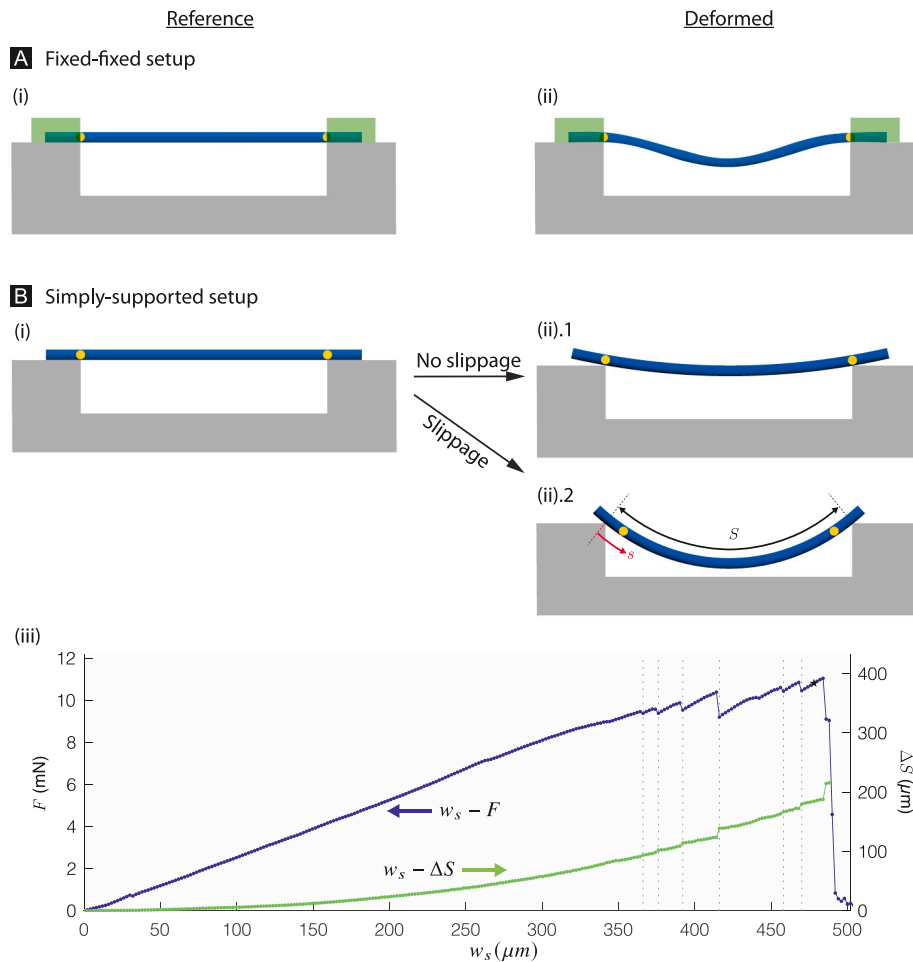


Fig. 3. Fixed-fixed setup and spicule slippage in simply-supported setup. (A)(i) shows the reference configuration of a spicule set up for a flexural test in a fixed-fixed setup; the spicule ends are glued onto the test's supports (adhesive shown in green). The yellow circles mark two spicule material particle that sit at the test's supports in this configuration. (A)(ii) shows the spicule in its deformed configuration as it is being tested with its ends glued to the test's supports. The material particles that were at the test's supports in the reference configuration (yellow circles) are still at the test's supports. (B)(i) shows a spicule in its reference configuration in the simply-supported setup. The yellow circles mark two spicule material particle that sit at the test's supports in this configuration. (B)(ii).1 shows a deformed spicule configuration in which the spicule has not undergone any slipping at the supports; the material particles that were at the test's supports in the reference configuration (yellow circles) are still at the test's supports in this configuration as well. This is the assumption made in standard beam theories, such as the Euler–Bernoulli beam theory, when they are used to model three point bending tests. (B)(ii).2 shows a deformed configuration of the spicule in which the spicule has undergone slippage at the test's supports. The material particles denoted by the yellow circles are no longer at the test's supports, but have slipped down into the trench. The parameter S denotes the spicule's total length, which is the length of the section of the spicule specimen lying between the test's supports. (B)(iii) shows the measured force F (left axis) (for details of what we mean by force, F , see Section 3) and the change in the total length, ΔS (right axis), from a representative three point bending test carried out in the simply supported setup as a function of stage displacement, w_s , in blue and green, respectively. The vertical dashed lines indicate the instances at which the drops in the force take place. As can be noted from the graphs, the jumps in the spicule's total length take place at those very same instances.

Source: (Modified from Kochiyama et al. (2021)).

they are due to a combination of layer-fracture events and slip-events, or (iii) they are entirely due to the slip-events.

To determine which of the three scenarios is likely true, three-point bending tests were carried out on the spicules again in the fixed-fixed (FF) setup (see Fig. 3(A)). In the FF setup, the spicule's ends are glued to the test's supports, which prevents the occurrence of any slip-events at the test's supports. None of the force–displacement curves from the FF tests displayed a sawtooth pattern. Although this observation points to scenario (iii) as being true, it is with the implicit assumption that the operation of the Cook–Gordon mechanism would be unaffected regardless of whether or not the spicule ends are free to slide and rotate. Since such an assumption is not explicitly validated, additional experiments were performed to gauge the likelihood of each of the three scenarios in an alternative manner. To be specific, the three-point bending tests were carried out on the spicules again in the SS setup, but the spicules were only loaded until a few force drops that are characteristic of the sawtooth-pattern were observed instead of until complete failure. The specimens were then unloaded until they

regained their straight shape and the force on them almost vanished. Finally, the spicules were loaded for the second time (re-loaded) until a few force drops were again observed. If the sawtooth pattern observed during the loading phase was due to the Cook–Gordon mechanism, then the spicule's stiffness (slope of the initial linear portion of the force–displacement curve before the appearance of the force drops) from the re-loading (second loading) phase should be different from that in the loading (first loading) phase. However, the spicules' stiffnesses in the loading and the re-loading phases were found to be almost the same. This observation implies that the force-drops in the loading phases are not due to the Cook–Gordon mechanism, which leads us to conclude that scenario (iii) is the one that is true.

In this paper, with the goal of further investigating our hypothesis, we develop and study a mechanics model for the spicule's SS bending tests. A distinguishing feature of our model is that the test specimen is allowed to slide at the test's supports. In contrast, in the standard Euler–Bernoulli (EB) model of the three point bending test, the specimen is not allowed to slide at the test's supports.

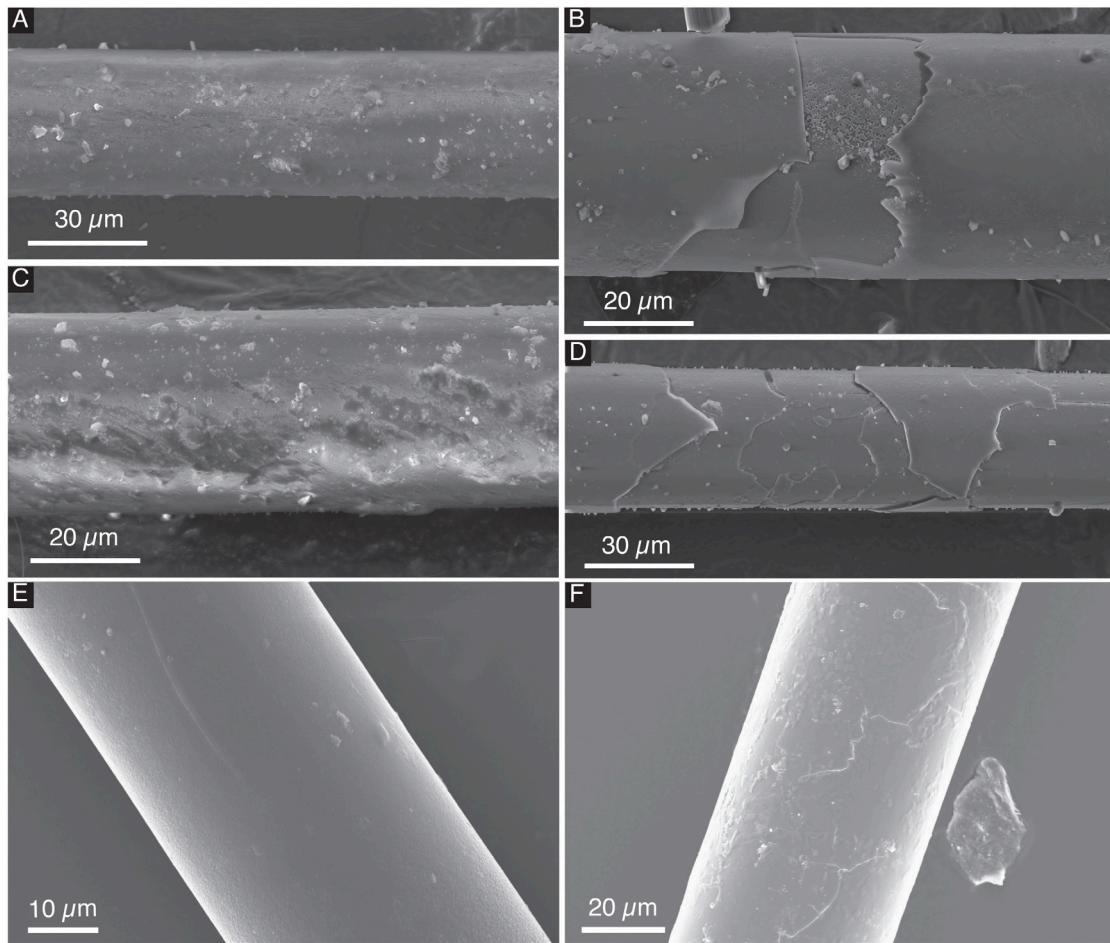


Fig. 4. Representative SEM images of a few randomly selected *E. aspergillum* spicules that were taken after the spicules had been flexurally tested in a simply-supported setup. Each spicule is identified by the label given to the flexural test (see Tables S1–S2 of Kochiyama et al. (2021) for detailed information pertaining to a given test) in which it was used. (A) and (B) are two different images of the spicule from the test SS4. (C)–(F) are images of the spicules from the tests SS7, SS24, SS32, and SS34, respectively. The imaged region in each spicule was chosen randomly. These images demonstrate how the spicules can have rough surfaces, as shown in (A)–(D), or relatively smooth surfaces, as shown in (E)–(F).

Considering the geometry in the SS experiments (e.g., see Fig. 2), in our model, the spicule's displacements are taken to be two dimensional in nature. The spicules are modeled as 1D continua considering their high aspect ratios (length:diameter) of ≈ 25 , and their bending behavior is modeled using Euler's elastica theory since they undergo large displacements in the experiments. Any stretching behavior along their axes are ignored. The contact at the test's supports is modeled using the Coulomb friction model. Scanning electron microscopy (SEM) revealed that the spicules' surfaces could have both smooth and rough regions. By roughness, we are referring to the different types of imperfections, including debris, scrapes and outer layer damage, that were observed on the spicules' surfaces (Fig. 4). We incorporate the spicules' surface roughness in our model by assuming that the coefficient of friction between the spicule and the test's supports varies depending on which particular spicule cross-section is in contact with the supports. Specifically, in the model it is assumed that the coefficient of friction varies along the spicule's length as

$$\mu_0 \left(1 + A \cos \left(\frac{2\pi s}{\lambda} - \phi \right) \right), \quad (1.1)$$

where s is the arc-length coordinate along the spicule's axis (see Fig. 3(B)(ii).2), and we refer to the parameters μ_0 , A , λ , and ϕ as the average value of coefficient of friction, the amplitude, the wavelength, and the phase, respectively. In our problem, the static and kinetic coefficients of friction are taken to have the same value. In Section 4.1, we present the governing equations of our model. In Section 4.2, we semi-analytically solve the governing equations to derive what we call our

model's equilibrium force–displacement curve. Each point on that curve corresponds to a static equilibrium configuration. Our model predicts that any measured force–displacement point will lie on the equilibrium curve. However, due to the finite stiffness of the loading apparatus, not all the points on the equilibrium curve will be measured in an experiment. Taking into account the stability of the equilibrium points in Section 4.3, we provide an algorithm for numerically determining our model's prediction for the force–displacement curve that will be measured in an SS experiment.

In Section 5, we compare the force–displacement curves predicted by our models with the ones that were experimentally measured in Monn and Kesari (2017), Kochiyama et al. (2021). We find that not only do the predicted force–displacement curves capture the sawtooth pattern, but they can also be made to quantitatively match the measured force–displacement remarkably well by appropriately choosing the value of μ_0 , A , λ , and ϕ . The sawtooth pattern in our model is a direct consequence of the slip events at the supports. We find that the values of μ_0 , which were chosen to match our model's prediction with the experimental measurements as closely as possible, is quite consistent with the values reported in literature for the coefficient of friction between glass and steel (note that the contact in the spicule SS experiments is between silica (spicule) and stainless steel (test's supports)).

Since the sawtooth pattern in our model is a direct consequence of slip events, the good match between our model's predictions and the experimental measurements supports our hypothesis that the sawtooth

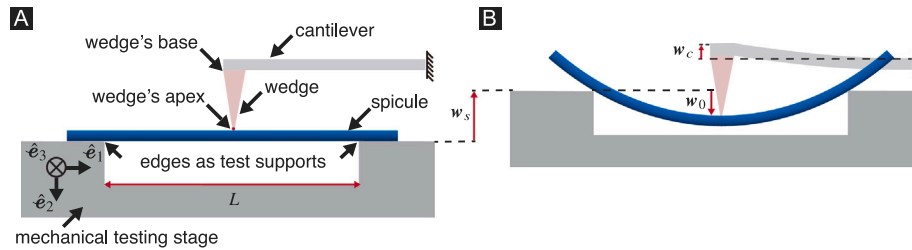


Fig. 5. An illustration of the simply-supported setup. (A) Schematic of the experimental setup used in our recent study (Kochiyama et al., 2021) for testing spicules in a simply-supported setup. The mechanical testing stage consisted of a stainless steel plate with a L μm wide trench, where the trench edges served as the test's supports. The loading device consisted of a wedge attached to a cantilever; to ensure that the cantilever's right end remained fixed in space during the experiment, the right end was encastered into a rigid aluminum frame (not shown in the schematic) that was independent of all the other testing structures. (B) Schematic of a simply-supported spicule in our experiment, which is being deformed under some applied load. The loading of the spicules was achieved by displacing the mechanical testing stage by w_s μm ($w_s = -w_s \hat{e}_2$) as shown, where the mechanical testing stage was mounted onto a three-axis motorized translation stage (not shown in the schematic) to enable precise control of its motion. As a result, the midpoint of the spicule is deflected by w_0 μm ($w_0 = w_0 \hat{e}_2$) and the free end of the cantilever is deflected by w_c μm ($w_c = -w_c \hat{e}_2$). For more details on the experiments see Section 3.

patterns in the experiments of Monn and Kesari are solely a consequence of the slip instabilities that take place at the trench's edges. However, the modeling results we put forward in this paper do not conclusively prove our hypothesis. This is because we were unable to check the reasonableness of the values we chose for the parameters A and λ while we were comparing our model to the experiments. We discuss this limitation of our current work in the concluding section of this paper, Section 6, where we also discuss a potential future direction for addressing this limitation.

We begin by discussing some mathematical notions that are needed for the development of our model. Following that we recapitulate the experimental setup of the SS bending tests in Section 3 before presenting our model in Section 4.

2. Mathematical preliminaries

The mathematical notions that we use in this paper are discussed in Kochiyama et al. (Section 2.1, 2021). However, for the readers' convenience, we briefly review some of those notions in this section.

We assume that our experiments take place in the three dimensional physical point space \mathcal{E} , and take \mathbb{E} to be a three dimensional, oriented, Hilbert space, such that \mathcal{E} is \mathbb{E} 's principle homogeneous space. We introduce vectors \hat{e}_1 , \hat{e}_2 , and \hat{e}_3 , as shown in Fig. 5(C), to form a basis for \mathbb{E} . We denote the dot product between any two vectors u and v as $u \cdot v$, where by definition $u \cdot v \in \mathbb{R}$, and \mathbb{R} is the set of all real numbers. The vectors \hat{e}_1 , \hat{e}_2 , and \hat{e}_3 are orthonormal. This can be expressed by stating that $\hat{e}_i \cdot \hat{e}_j = \delta_{ij}$, where $i, j \in (1, 2, 3)$, and the Kronecker delta symbol δ_{ij} is defined as having a value of unity if $i = j$ and zero otherwise.

Following Rahaman et al. (2020), we consider vectors to carry units with them if they belong to a physical vector space. For instance, we take that \hat{e}_i , $i \in (1, 2, 3)$, carry the units of μm (micrometers). The magnitude/norm of the vector u is denoted as $\|u\| = (u \cdot u)^{1/2}$. The norm $\|u\|$ is non-dimensional, or to be more precise, $\|u\| \in \mathbb{R}_{\geq 0}$, where $\mathbb{R}_{\geq 0}$ is the set of non-negative real numbers.

Following Rahaman et al. (2020) and Deng and Kesari (2021), we model force as a linear map from \mathbb{E} into the one dimensional vector space whose elements carry units of energy. Let the forces \hat{f}_i , $i \in (1, 2, 3)$, be defined such that $\hat{f}_i(\hat{e}_j) = \delta_{ij}$ nJ (10^{-9} Joules), where \hat{f}_i is a milli-newton of force acting in the \hat{e}_i direction. The set of all forces can be made into a vector space \mathbb{F} by defining the addition between two forces u and v to be the force w such that $w(x) = u(x) + v(x)$ for all $x \in \mathbb{E}$. Let \mathfrak{F} be the linear map from \mathbb{E} to \mathbb{F} such that $\mathfrak{F}(\hat{e}_i) = \hat{f}_i$. Then, defining the dot product between forces u and v to be the dot product in \mathbb{E} between the vectors $\mathfrak{F}^{-1}(u)$ and $\mathfrak{F}^{-1}(v)$, where \mathfrak{F}^{-1} is the inverse of \mathfrak{F} , the space \mathbb{F} can be made into a Hilbert space. It can be shown that $(\hat{f}_i)_{i \in (1, 2, 3)}$ provides an orthonormal basis for \mathbb{F} .

3. A brief review of the simply supported, three-point bending experiments from Part I

In this section we briefly recall the set-up of the simply-supported (SS) experiments mentioned in Section 1.

A trench of width L μm was cut into a stainless steel mechanical testing stage (MTS) (see Fig. 5(C)). The non-dimensional trench width L was 1278 ± 3 (mean \pm standard deviation) in the experiments. Spicules were placed across the trench with their lengths parallel to the \hat{e}_1 direction so that initially, the spicule's cross-sections were normal to \hat{e}_1 . The trench's edges, which run parallel to the \hat{e}_3 direction, served as the test's supports. A cantilever with a wedge attached to it was positioned over the spicule. The wedge's triangular faces were normal to the \hat{e}_3 direction with the triangle's base normal to the $-\hat{e}_2$ direction and facing away from the spicule, and the triangle's apex facing the spicule. At the beginning of the experiment, the wedge's apex (shown marked in Fig. 5(C)) was just above the spicule's midpoint, i.e., over the spicule cross-section that lay midway across the trench. The cantilever and the wedge were made of either steel or aluminum.

The loading phase of the tests were conducted by moving the MTS in the $-\hat{e}_2$ direction at a rate of 1 $\mu\text{m}/\text{s}$. The MTS was driven by a DC servo motor, whose motion was controlled through a PID algorithm. The stage was moved in 2 μm increments. During the increment, the stage's velocity was maintained between 50 and 200 $\mu\text{m}/\text{s}$. Thus, each stage increment took anywhere between 10 and 40 ms. After each increment, the stage was held motionless so that there was a 2100 ms time interval between the starting points of any two consecutive increments. Each data point that we report was calculated using the average value of the sensor readings collected over the last 100 ms of each of those time intervals.

We denote an arbitrary time instance during the experiment as τ ms, where $\tau \in [0, \tau^*]$. The time $\tau = 0$ corresponds to the instance at which the spicule first makes contact with the wedge's apex, and the time $\tau = \tau^* > 0$ corresponds to the instance when the spicule fails. We express the MTS's displacement as $-w_s(\tau)\hat{e}_2$. Here, $w_s(\tau) \in \mathbb{R}$ is a known non-dimensional quantity since the stage's displacement was an input in our experiment.

As the stage moved upwards ($-\hat{e}_2$ direction) the spicule made contact with the wedge's apex and got deflected into the trench, while the cantilever got deflected away from the trench. We express the cantilever's wedge's motion as $-w_c(\tau)\hat{e}_2$ (compare Fig. 5(C) and (D)). Here, $w_c(\tau)$ is the non-dimensional cantilever displacement, which is defined as the dot product between $-\hat{e}_2$ and the wedge's displacement vector at the time instance τ . We denote the spicule's midpoint deflection, or simply displacement, as $w_0(\tau)\hat{e}_2$, where $w_0(\tau) \in \mathbb{R}$ is the dot product between \hat{e}_2 and the displacement vector of the centroid of the spicule's cross-section that is directly underneath the wedge's apex. It can be shown that the quantities $w_s(\tau)$, $w_c(\tau)$, and $w_0(\tau)$ are related as

$$w_s(\tau) = w_c(\tau) + w_0(\tau). \quad (3.1)$$

In terms of

$$\hat{w}_s(\tau) := \frac{w_s(\tau)}{L}, \quad (3.2a)$$

$$\hat{w}_c(\tau) := \frac{w_c(\tau)}{L}, \quad (3.2b)$$

$$\hat{w}_0(\tau) := \frac{w_0(\tau)}{L}, \quad (3.2c)$$

Eq. (3.1) reads

$$\hat{w}_s(\tau) = \hat{w}_c(\tau) + \hat{w}_0(\tau). \quad (3.3)$$

Let $F(\tau)$ be the force acting on the spicule's midpoint. We assume that the wedge's apex only applies force in the $\pm \hat{e}_2$ directions. This allows us to express

$$F(\tau) = F(\tau) \hat{f}_2, \quad (3.4)$$

where $F(\tau) \in \mathbb{R}$ is a non-dimensional quantity. We model the cantilever as a linear spring that is oriented in the \hat{e}_2 direction and having a stiffness of $\hat{k}_c = k_c$ mN/ μ m. From this model, it follows that

$$F(\tau) = k_c w_c(\tau). \quad (3.5a)$$

We measured k_c independently, using a procedure unrelated to the SS experiments, and found it to vary from 86.4 to 90.1 (see Tables S1–S2 of Kochiyama et al. (2021)). The constitutive law expressed by (3.5a) can alternately be written as

$$\hat{F}(\tau) = \hat{k}_c \hat{w}_c(\tau), \quad (3.5b)$$

where

$$\hat{F}(\tau) := \frac{F(\tau)L^2}{EI}, \quad (3.6a)$$

$$\hat{k}_c := \frac{k_c L^3}{EI}, \quad (3.6b)$$

E mN/ μ m² is the spicule specimen's Young's modulus, and I μ m⁴ is the spicule specimen's bending moment of inertia.

In each experiment, we measured the function $\mathbb{R}_{\geq 0} \ni \tau \mapsto w_c(\tau) \in \mathbb{R}$. Since we knew k_c , on account of (3.2b) and (3.5b), this was tantamount to measuring the function $\tau \mapsto \hat{F}(\tau)$. Additionally, since we know $w_s(\cdot)$, using the measured $w_c(\cdot)$ along with (3.2a), (3.2b), and (3.3), we can construct $\tau \mapsto \hat{w}_0(\tau)$. We call the map

$$\tau \xrightarrow{\gamma_m} (\hat{w}_0(\tau), \hat{F}(\tau)), \quad (3.7)$$

the measured force–displacement curve.

4. Theory

The goal of the model we develop in this section is to provide a prediction for the measured force–displacement curves in the loading phase of the SS experiments.

4.1. Equations governing the spicule's equilibrium configurations

We denote the total length of the spicule specimen lying between the supports in the deformed configuration S μ m (see Fig. 3(B)(ii).1). We take our problem to be completely symmetric about the trench's mid-plane. For a given total spicule length, S , we define a spicule's equilibrium configuration to be a kinematically admissible spicule deformation map and a spicule-trench edge contact force. The map should be such that the net force and the moment vanish on every one of the spicule's material regions; the contact force should be such that it satisfies the prescribed contact constitutive law between the spicule and the trench.

4.1.1. Euler's elastica theory

We assume the spicule to be inextensible. Thus, S denotes the total length of the spicule specimen lying between the supports in its reference configuration as well. We call the length of the spicule-section lying between a spicule material particle on the spicule's central axis and the spicule cross-section contacting the trench's left edge the particle's arc-length coordinate $s \in (0, S)$ (see Fig. 3(B). (ii).2). When there is no risk of confusion, we will henceforth be referring to a spicule material particle lying on the spicule's central axis simply as a spicule material particle. We call

$$\hat{s} := s/S, \quad (4.1)$$

the particle's scaled arc-length coordinate. We identify a spicule material particle with either its arc-length or scaled arc-length coordinate.

As mentioned before, we assume that our problem is completely symmetric about the trench's mid-plane, i.e., the plane perpendicular to \hat{e}_1 and containing the point $(L/2, 0, 0)$. Therefore, the spicule's deformed shape can be described using the (scaled) deformation mapping

$$\hat{\alpha}(\cdot) : (0, 1/2) \rightarrow \mathbb{E}, \quad (4.2a)$$

where

$$\hat{\alpha}(\cdot) = \frac{\alpha(\cdot)}{L}, \quad (4.2b)$$

and $\alpha(\xi)$ is the position vector of the spicule material particle whose arc-length coordinate is ξS .

We can define a Frenet–Serret frame (Forsyth, 1912) corresponding to the curve $\hat{\alpha}(\cdot)$ at each spicule material particle. The unit tangent and normal vectors in that frame at the material particle \hat{s} can be computed as

$$\hat{e}_t(\hat{s}) = \hat{\alpha}'(\hat{s}) / \|\hat{\alpha}'(\hat{s})\|, \quad (4.3a)$$

$$\hat{e}_n(\hat{s}) = \hat{e}_t'(\hat{s}) / \|\hat{e}_t'(\hat{s})\|, \quad (4.3b)$$

respectively, where $\hat{\alpha}'(\cdot)$ is the derivative of $\hat{\alpha}(\cdot)$, and $\hat{e}_t'(\cdot)$ is the derivative of $\hat{e}_t(\cdot)$. Using the definition of s , Eqs. (4.1), and (4.2), it can be shown that $\|\hat{\alpha}'(\hat{s})\| = \hat{S}$, where

$$\hat{S} = \frac{S}{L}. \quad (4.4)$$

Let $\theta(\cdot) : (0, 1/2) \rightarrow (-\pi, \pi]$ be defined such that $\theta(\hat{s})$ is the angle between \hat{e}_1 and $\hat{e}_t(\hat{s})$ ¹ (see Fig. 6(A)). We can express $\hat{e}_t(\hat{s})$, $\hat{e}_n(\hat{s})$ using $\theta(\hat{s})$ as

$$\hat{e}_t(\hat{s}) = \cos(\theta(\hat{s}))\hat{e}_1 + \sin(\theta(\hat{s}))\hat{e}_2, \quad (4.5a)$$

$$\hat{e}_n(\hat{s}) = \sin(\theta(\hat{s}))\hat{e}_1 - \cos(\theta(\hat{s}))\hat{e}_2, \quad (4.5b)$$

respectively. Let $EI\hat{P}(\hat{s})/L^2 \in \mathbb{F}$ be the force acting on the spicule cross-section containing the spicule material particle \hat{s} . Specifically, $EI\hat{P}(0)/L^2$ is the force acting on the spicule due to its contact with the trench's left edge. The vector $\hat{P}(0)$ can be expressed as

$$\hat{P}(0) = \hat{P}_1 \hat{f}_1 + \hat{P}_2 \hat{f}_2, \quad (4.6)$$

where $\hat{P}_1, \hat{P}_2 \in \mathbb{R}$.

The spicule's high aspect ratio and the observation of large displacements in our SS experiments motivates us to use the Euler's elastica theory (Euler, 1952; Timoshenko and Gere, 2009) to model the spicule's deformation. The elastica theory is an extension of the EB theory to the regime of large displacements and rotations. As per the elastica theory,

¹ To be clear, considering two vectors of unit magnitude $a := a_1 \hat{e}_1 + a_2 \hat{e}_2$ and $b := b_1 \hat{e}_1 + b_2 \hat{e}_2$, the angle between them is the real number θ in $(-\pi, \pi]$ such that $a_1 \cos(\theta) - a_2 \sin(\theta) = b_1$ and $a_2 \cos(\theta) + a_1 \sin(\theta) = b_2$.

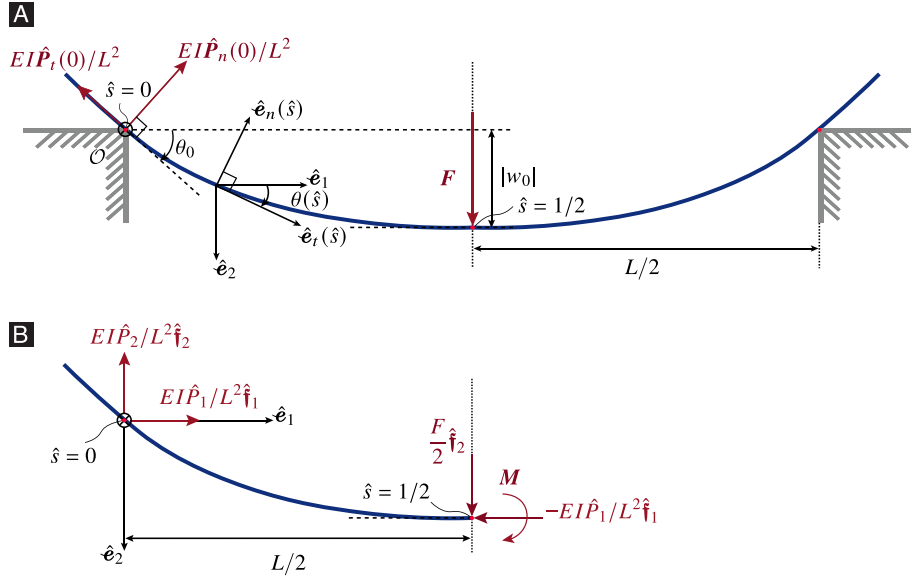


Fig. 6. Geometry in our mechanics model. (A) A schematic of a beam (blue) suspended over a trench (gray). At $\hat{s} = 0$ the beam experiences the normal reaction force $EI \hat{P}_n(0)/L^2$ and the frictional reaction force $EI \hat{P}_t(0)/L^2$. The force F acts at the spicule midpoint. The magnitude of the beam's midpoint's deflection is $|w_0|$. The angle between \hat{e}_1 and $\hat{e}_r(\hat{s})$ is $\theta(\hat{s})$, and $\theta_0 := \theta(0)$. (B) A free body diagram of the left half of the beam (blue). The beam is subject to the forces $EI \hat{P}_1/L^2 \hat{f}_1$, and $EI \hat{P}_2/L^2 \hat{f}_2$ at $\hat{s} = 0$, and the forces $-EI \hat{P}_1/L^2 \hat{f}_1$, and $F/2 \hat{f}_2$ at $\hat{s} = 1/2$. At $\hat{s} = 1/2$ the beam is also subject to a moment M .

the spicule's cross-sectional rotation $\theta(\cdot)$ needs to satisfy the non-linear differential equation

$$\theta''(\hat{s})/\hat{S}^2 + \hat{P}_1 \sin(\theta(\hat{s})) - \hat{P}_2 \cos(\theta(\hat{s})) = 0, \quad (4.7a)$$

over the domain $(0, 1/2)$ and satisfy the boundary conditions

$$\theta'(\hat{s})|_{\hat{s}=0} = 0, \quad (4.7b)$$

$$\theta(\hat{s})|_{\hat{s}=1/2} = 0. \quad (4.7c)$$

In (4.7), $\theta'(\cdot)$ and $\theta''(\cdot)$ denote $\theta(\cdot)$'s first and second derivatives, respectively. The boundary condition (4.7b) follows from the fact that there is no bending moment acting on the spicule at $\hat{s} = 0$, and the boundary condition (4.7c) follows from the problem's symmetry about the trench's mid plane.

4.1.2. Coulomb friction model

Let

$$\hat{f}_t(\hat{s}) := \mathfrak{F}(\hat{e}_r(\hat{s})) = \cos(\theta(\hat{s}))\hat{f}_1 + \sin(\theta(\hat{s}))\hat{f}_2, \quad (4.8a)$$

$$\hat{f}_n(\hat{s}) := \mathfrak{F}(\hat{e}_n(\hat{s})) = \sin(\theta(\hat{s}))\hat{f}_1 - \cos(\theta(\hat{s}))\hat{f}_2. \quad (4.8b)$$

The linear map \mathfrak{F} appearing in (4.8) has been defined in Section 2. Using $\hat{f}_t(\hat{s})$, $\hat{f}_n(\hat{s})$, we can express $\hat{P}(\hat{s})$ as the sum of $\hat{P}_t(\hat{s})$ and $\hat{P}_n(\hat{s})$, where $\hat{P}_t(\hat{s}) = \hat{P}(\hat{s})\hat{f}_t(\hat{s})$, $\hat{P}_n(\hat{s}) = \hat{P}(\hat{s})\hat{f}_n(\hat{s})$, and $\hat{P}_t(\cdot)$, $\hat{P}_n(\cdot) : (0, 1/2) \rightarrow \mathbb{R}$. We refer to $\hat{P}_t(\hat{s})$ and $\hat{P}_n(\hat{s})$ as, respectively, the (scaled) tangential and normal forces at the material particle \hat{s} . We call $\hat{P}_t(0)$ and $\hat{P}_n(0)$ the (scaled) tangential and normal contact forces (at the left trench edge), respectively, and for brevity, denote their magnitudes, i.e., $\hat{P}_t(0)$ and $\hat{P}_n(0)$, as \hat{P}_t and \hat{P}_n , respectively.

We define the angle $\beta_0 \in (0, \pi)$ such that

$$\cot(\beta_0) = \frac{\hat{P}_t}{\hat{P}_n}. \quad (4.9)$$

It follows from Eqs. (4.6), (4.8), and (4.9), and the definitions of \hat{P}_t and \hat{P}_n that

$$\hat{P}_1 = \hat{P}_n \csc(\beta_0) \cos(\theta_0 - \beta_0), \quad (4.10a)$$

$$\hat{P}_2 = \hat{P}_n \csc(\beta_0) \sin(\theta_0 - \beta_0), \quad (4.10b)$$

where

$$\theta_0 := \theta(0). \quad (4.10c)$$

Substituting \hat{P}_1 , \hat{P}_2 from (4.10) into (4.7a) and simplifying, we get that

$$\theta''(\hat{s}) + \hat{S}^2 \hat{P}_n \csc(\beta_0) \sin(\theta(\hat{s}) - \theta_0 + \beta_0) = 0. \quad (4.11)$$

We model contact between the spicule and the trench edges using the Coulomb's law of friction (Popov, 2017). As per the Coulomb's law, when $\hat{P}_n \geq 0$, $|\hat{P}_t| \leq \mu \hat{P}_n$, which in terms of β_0 reads

$$-\mu \leq \cot(\beta_0) \leq \mu. \quad (4.12)$$

where μ is the coefficient of friction. (As we mentioned in Section 1, in our problem we take the static and kinetic coefficients of friction to have the same value).

4.2. Equilibrium force–displacement curves

4.2.1. Solution to the boundary value problem (4.7) using the solution to the nonlinear pendulum problem

Following Blasius (for accessible references, see, e.g., Goldstein, 1938; Klamkin, 1962), we construct the solution to our boundary value problem (BVP) (4.7) using the solution of an auxiliary initial value problem (IVP).

The IVP we consider is as follows. The function $\beta : (0, 1/2) \rightarrow (-\pi, \pi]$ satisfies the nonlinear ordinary differential equation (ODE)

$$\beta''(\hat{s}) + \omega^2 \sin(\beta(\hat{s})) = 0, \quad (4.13a)$$

and the initial conditions

$$\beta(\hat{s})|_{\hat{s}=0} = \beta_0, \quad (4.13b)$$

$$\beta'(\hat{s})|_{\hat{s}=0} = 0, \quad (4.13c)$$

where $\omega > 0$ and $\beta_0 \in (0, \pi)$. The IVP (4.13) is related to the problem of a simple pendulum executing finite angle motions in a

plane. The complete solution to the IVP (4.13) is commonly attributed to Euler (Euler, 1750). For more modern references of the solution, see, e.g., Whittaker (1937), Beléndez et al. (2007). In order to explicitly note the dependence of the solution to the IVP (4.13), i.e., $\beta(\cdot)$, on the parameters ω and β_0 , we denote $\beta(\cdot)$ in the remainder of this paper as $\beta(\cdot; \omega, \beta_0)$ and express it as

$$\beta(\hat{s}; \omega, \beta_0) = 2 \arcsin \left(\sin \frac{\beta_0}{2} \operatorname{cd} \left(\omega \hat{s}; \sin^2 \frac{\beta_0}{2} \right) \right), \quad (4.14)$$

where $\operatorname{cd}(u; m) := \cos(\psi(u; m)) (1 - m \sin^2(\psi(u; m)))^{-1/2}$ is the Jacobi elliptic function. Here, $\psi(u; m)$ is the Jacobi amplitude, which is the inverse of the elliptic integral of the first kind, i.e., ψ, u, m satisfy the equation $u = \int_0^\psi (1 - m^2 \sin^2(\zeta)^2)^{-1/2} d\zeta$.

It can be shown that the solution to our BVP, $\theta(\cdot)$, can be constructed using $\beta(\cdot; \omega, \beta_0)$ as

$$\theta(\hat{s}) = \beta(\hat{s}; \omega(\hat{S}, \hat{P}_n, \beta_0), \beta_0) - \beta\left(\frac{1}{2}; \omega(\hat{S}, \hat{P}_n, \beta_0), \beta_0\right), \quad (4.15a)$$

where

$$\omega(\hat{S}, \hat{P}_n, \beta_0) := \hat{S} (\hat{P}_n \operatorname{csc}(\beta_0))^{1/2}. \quad (4.15b)$$

It can be deduced from (4.15) that $\theta(\cdot)$ depends on the independent parameters \hat{S} , \hat{P}_n , and β_0 . We will explicitly note this dependence by denoting $\theta(\cdot)$ as $\theta(\cdot; \hat{S}, \hat{P}_n, \beta_0)$. In order to make our results look less cumbersome, we will denote the sequence of independent parameters \hat{S} , \hat{P}_n , and β_0 simply as \mathbf{p} . In terms of \mathbf{p} , the solution $\theta(\cdot; \hat{S}, \hat{P}_n, \beta_0)$ will appear as $\theta(\cdot; \mathbf{p})$, and the result (4.15) will read

$$\theta(\hat{s}; \mathbf{p}) = \beta(\hat{s}; \omega(\mathbf{p}), \beta_0) - \beta\left(\frac{1}{2}; \omega(\mathbf{p}), \beta_0\right), \quad (4.16a)$$

where

$$\omega(\mathbf{p}) := \hat{S} (\hat{P}_n \operatorname{csc}(\beta_0))^{1/2}. \quad (4.16b)$$

4.2.2. Midpoint deflection and force

In this section, we present formulae for calculating the midpoint deflection \hat{w}_0 and force \hat{F} . As we did with $\theta(\cdot)$, when we want to note the dependence of \hat{w}_0 , \hat{F} , θ_0 , and $\hat{\alpha}(\cdot)$ on the independent parameters \hat{S} , \hat{P}_n , and β_0 explicitly, we will denote them as $\hat{w}_0(\mathbf{p})$, $\hat{F}(\mathbf{p})$, $\theta_0(\mathbf{p})$ and $\hat{\alpha}(\cdot; \mathbf{p})$, respectively.

We can express $\hat{\alpha}(\hat{s}; \mathbf{p})$ as $\hat{x}_1(\hat{s}; \mathbf{p})\hat{e}_1 + \hat{x}_2(\hat{s}; \mathbf{p})\hat{e}_2$, where $\hat{x}_1(\cdot; \mathbf{p})$, $\hat{x}_2(\cdot; \mathbf{p})$ are smooth real valued functions on $(0, 1/2)$. It follows from (4.3a) and (4.5a) that

$$\hat{x}'_1(\hat{s}; \mathbf{p}) = \hat{S} \cos(\theta(\hat{s}; \mathbf{p})), \quad (4.17a)$$

$$\hat{x}'_2(\hat{s}; \mathbf{p}) = \hat{S} \sin(\theta(\hat{s}; \mathbf{p})). \quad (4.17b)$$

Midpoint deflection. Integrating (4.17b) from $\hat{s} = 0$ to $\hat{s} = 1/2$, simplifying the expression $\int_0^{1/2} \hat{x}'_2(\hat{s}; \mathbf{p}) d\hat{s}$ that appears on the left hand side (LHS) of the resulting equation as $\hat{x}_2(1/2; \mathbf{p}) - \hat{x}_2(0; \mathbf{p})$, and then noting that $\hat{x}_2(1/2; \mathbf{p}) = \hat{w}_0(\mathbf{p})$ and $\hat{x}_2(0; \mathbf{p}) = 0$, we get that

$$\hat{w}_0(\mathbf{p}) = \hat{S} \int_0^{1/2} \sin(\theta(\hat{s}; \mathbf{p})) d\hat{s}. \quad (4.18)$$

Midpoint force. From the balance of external forces acting on the left half of the spicule specimen (Fig. 6(B)) in the \hat{j}_2 direction, we get that

$$\hat{F} + 2\hat{P}_2 = 0. \quad (4.19)$$

Substituting \hat{P}_2 in (4.19) from (4.10b) and then using (4.16b) and substituting the factor $\hat{P}_n \operatorname{csc}(\beta_0)$ as $\omega(\mathbf{p})^2/\hat{S}^2$, we get

$$\hat{F}(\mathbf{p}) = -2\omega(\mathbf{p})^2 \sin(\theta_0(\mathbf{p}) - \beta_0) \frac{1}{\hat{S}^2}. \quad (4.20)$$

Integrating (4.17a) from $\hat{s} = 0$ to $\hat{s} = 1/2$, simplifying the expression $\int_0^{1/2} \hat{x}'_1(\hat{s}; \mathbf{p}) d\hat{s}$ that appears on the LHS as $\hat{x}_1(1/2; \mathbf{p}) - \hat{x}_1(0; \mathbf{p})$, noting that $\hat{x}_1(1/2; \mathbf{p}) = 1/2$ and $\hat{x}_1(0; \mathbf{p}) = 0$, multiplying the resulting equation with $2/\hat{S}$, and then squaring the result, we get that

$$\frac{1}{\hat{S}^2} = 4 \left(\int_0^{1/2} \cos(\theta(\hat{s}; \mathbf{p})) d\hat{s} \right)^2. \quad (4.21)$$

Substituting the factor $1/\hat{S}^2$ in (4.20) from (4.21) and simplifying, we get that

$$\hat{F}(\mathbf{p}) = 8\omega(\mathbf{p})^2 \left(\int_0^{1/2} \cos(\theta(\hat{s}; \mathbf{p})) d\hat{s} \right)^2 \sin(\beta_0 - \theta_0(\mathbf{p})). \quad (4.22)$$

4.2.3. Compatibility

Substituting $\theta(\cdot; \mathbf{p})$ in (4.21) from (4.16) and rearranging, we get

$$\hat{S} = \frac{1}{2} \left(\int_0^{1/2} \cos \left(\beta(\hat{s}; \omega(\mathbf{p}), \beta_0) - \beta\left(\frac{1}{2}; \omega(\mathbf{p}), \beta_0\right) \right) d\hat{s} \right)^{-1}. \quad (4.23)$$

4.2.4. Upper envelope of the equilibrium region and the closing equation

In order to derive our model's predictions for the force-displacement curves measured by the SS experiments in the loading phase, the spicule-specimen's equilibrium configurations first need to be extracted. We define what we physically mean by the spicule specimen's equilibrium configuration at the beginning of Section 4.1 (when the spicule specimen is in one of its equilibrium configurations, that does not necessarily mean that the MTS's cantilever wedge is also in one of its equilibrium configurations, i.e., that our entire mechanical system is in equilibrium. See Section 4.3 for further discussion of this issue). Mathematically, a spicule's equilibrium configuration can be described as an ordered set $(\hat{S}, \hat{P}_n, \beta_0)$ that satisfies the contact constitutive law (4.12) and the compatibility condition (4.23). We mark the equilibrium configurations, which were determined numerically using Algorithm 1, in the \hat{w}_0 - \hat{F} , \hat{S} - \hat{w}_0 , and \hat{S} - \hat{F} spaces for a representative case in Figs. 7(A), (B), and (C), respectively. For a given \hat{S} , there can exist more than one equilibrium configuration. This is partly because as can be seen from (4.9) and (4.12), the number $\cot(\beta_0)$ only needs to lie between certain bounds, specifically between $\pm\mu$. Therefore, in general, the sets of equilibrium states have non-zero measures in the \hat{w}_0 - \hat{F} , \hat{S} - \hat{w}_0 or \hat{S} - \hat{F} spaces.

However, it can be argued that in the loading portion of the SS experiments, $\hat{P}_n \geq 0$. Under some mild assumptions on the loading rate, it can be further argued² that $\cot(\beta_0)$ in fact achieves its lower bound, i.e., that

$$\cot(\beta_0) = -\mu. \quad (4.24)$$

As discussed in Section 1, it is reasonable to assume that μ varies along the spicule's length so that the value of μ depends on the contact position between the spicule and the trench's left edge, which depends on \hat{S} . We assume that the dependence of μ on \hat{S} can be expressed as

$$\mu(\hat{S}) = \mu_0 \left(1 + A \cos \left(\frac{\pi \hat{S}}{\lambda} + \phi \right) \right), \quad (4.25)$$

where $\hat{\lambda} := \lambda/L$, $\lambda \in \mathbb{R}_{\geq 0}$. Here, $\lambda \mu\text{m}$ is the wavelength of the assumed periodic variation of the coefficient of friction. Note that the value of the phase ϕ , depending on the positions of contacting points between the spicule specimens and the trench edges at the beginning of the experiments, may not be the same as the value of ϕ in (1.1).

Therefore, in an equilibrium state, the value of β_0 is fully determined by the value of \hat{S} in that state. More specifically, it follows from (4.24)

² The mathematical analysis underlying this assertion is quite involved and therefore we plan on publishing it elsewhere.

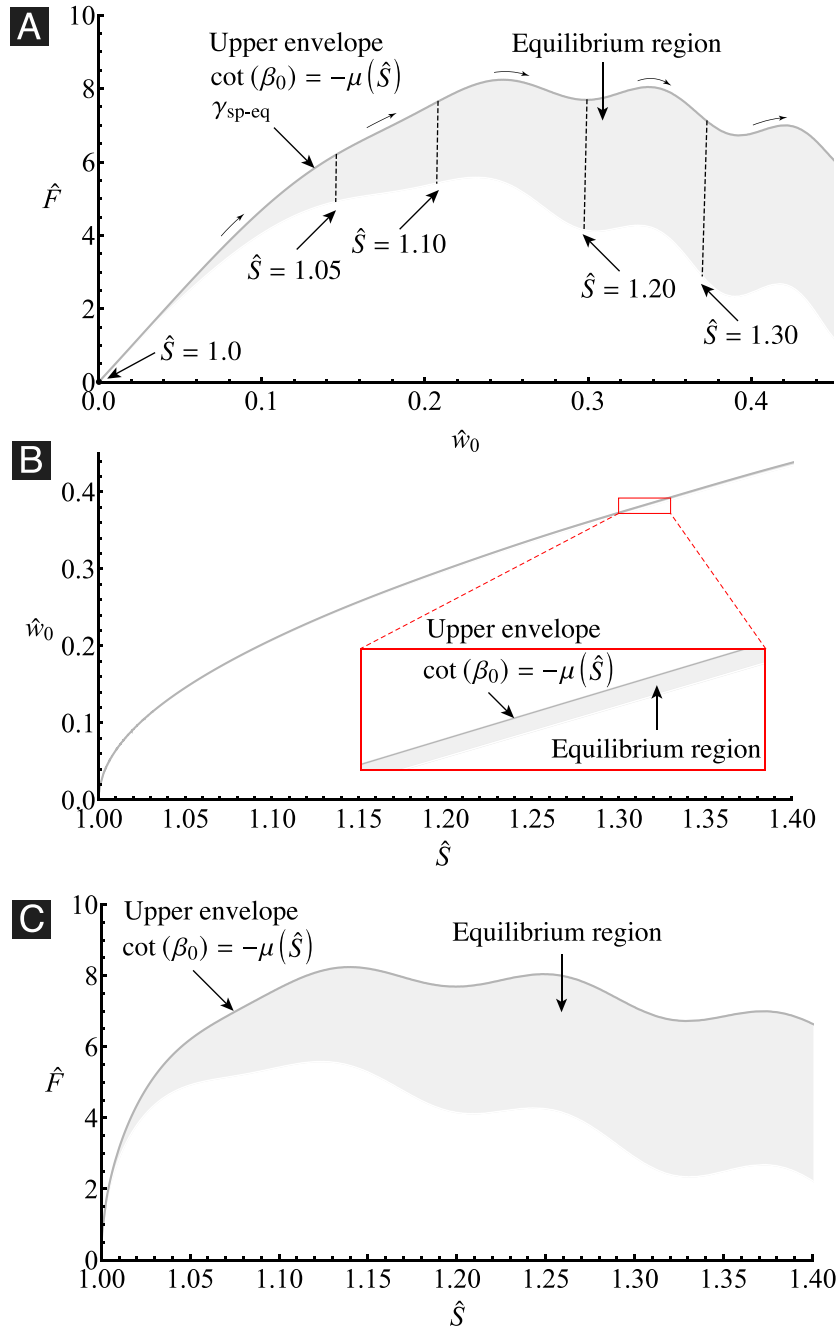


Fig. 7. The equilibrium region in the \hat{w}_0 - \hat{F} , \hat{S} - \hat{w}_0 , and \hat{S} - \hat{F} space for a representative case. We consider the case in which the coefficient of friction varies as in (4.25) with $\mu_0 = 0.3$, $A = 0.2$, $\hat{\lambda} = 0.02\pi$, and $\phi = 0$, i.e., in which $\mu(\hat{S}) = 0.3(1 + 0.2\cos(\hat{S}/0.02))$. For this case we computed the equilibrium regions using the procedure detailed in Algorithm 1. Subfigures (A), (B), and (C) show the equilibrium region in the \hat{w}_0 - \hat{F} , \hat{S} - \hat{w}_0 , and \hat{S} - \hat{F} space, respectively. In each of the subfigures the equilibrium region is shown in light gray, while the upper envelope of the equilibrium region (i.e., the equilibrium curve) is shown as a dark-gray curve. In (A) we mark a locus of configurations in which \hat{S} is constant using a dashed black curve. The solid arrows above the equilibrium curve indicate that \hat{S} strictly increases as we travel along the curve starting from the origin.

that β_0 is equal to the value of $\beta_0(\hat{S})$, where the function $\beta_0(\cdot) : [1, \infty) \rightarrow (0, \pi)$ is defined by equations

$$\sin(\beta_0(\hat{S})) = \frac{1}{\sqrt{1 + \mu(\hat{S})^2}}, \tag{4.26a}$$

$$\cos(\beta_0(\hat{S})) = \frac{-\mu(\hat{S})}{\sqrt{1 + \mu(\hat{S})^2}}. \tag{4.26b}$$

As mentioned in Section 1, for simplicity, we take $\mu(\cdot)$ to be of the form given by (4.25).

It now follows from (4.23) that in the state mentioned above, the value of \hat{P}_n is also fully determined by the value of \hat{S} ; the value of \hat{P}_n has to be a root of $f(\cdot; \hat{S}, \beta_0(\hat{S}))$, and the function $f(\cdot; \hat{S}, \beta_0) : \mathbb{R}_{\geq 0} \rightarrow \mathbb{R}$ is defined by equation

$$f(\cdot; \hat{S}, \beta_0) = 1 - 2\hat{S} \int_0^{1/2} \cos\left(\beta(\hat{s}; \omega(\hat{S}, \cdot, \beta_0), \beta_0) - \beta\left(\frac{1}{2}; \omega(\hat{S}, \cdot, \beta_0), \beta_0\right)\right) d\hat{s}. \tag{4.27}$$

In general, $f(\cdot; \hat{S}, \beta_0(\hat{S}))$ will have multiple roots. However, using practical considerations, it can be deduced that only the smallest

of $f(\cdot; \hat{S}, \beta_0(\hat{S}))$'s roots is relevant in the context of the SS experiments. We denote the value of that smallest root as $\hat{P}_n(\hat{S})$, which can be computed using the Newton–Raphson method.

The results put forward in the last three paragraphs can be summarized by stating that, during the loading portion of the SS experiments, the equilibrium states have the form $(\hat{S}, \hat{P}_n(\hat{S}), \hat{\beta}_0(\hat{S}))$. We call the set of the equilibrium states having this form the upper envelope of the equilibrium region (shown as gray curves in Fig. 7). The upper envelope of the equilibrium region in the \hat{w}_0 - \hat{F} space can be expressed as the parametric curve

$$\gamma_{\text{sp-eq}} := \{(\hat{w}_0^+(\hat{S}), \hat{F}^+(\hat{S})) \mid \hat{S} \geq 1\}, \quad (4.28a)$$

where $\hat{w}_0^+(\cdot) : [1, \infty) \rightarrow \mathbb{R}_{\geq 0}$ is defined by the equation

$$\hat{w}_0^+(\hat{S}) = \hat{w}_0(\hat{S}, \hat{P}_n(\hat{S}), \hat{\beta}_0(\hat{S})), \quad (4.28b)$$

and $\hat{F}^+ : [1, \infty) \rightarrow \mathbb{R}_{\geq 0}$ is defined by the equation

$$\hat{F}^+(\hat{S}) = \hat{F}(\hat{S}, \hat{P}_n(\hat{S}), \hat{\beta}_0(\hat{S})). \quad (4.28c)$$

We will be referring to $\gamma_{\text{sp-eq}}$ simply as the spicule equilibrium curve. The equilibrium curve can be numerically constructed using Algorithm 1 after changing line number 5 in it to “Compute $\beta_0^+ \leftarrow \text{arccot}(-\mu(\hat{S}))$, then $\beta_0^- \leftarrow \beta_0^+$ ”

Algorithm 1: Procedure for computing the equilibrium region.

- 1: **Input:** $\mu_0, A, \hat{\lambda}, \phi, \hat{S}^{*a}$, and natural numbers $n_{\hat{S}}$, and $n_{\beta_0}^b$
- 2: **Initialization:** $\hat{S} = 1, \hat{P}_n = 0, \hat{w}_0 = 0, \hat{F} = 0, \Delta\hat{S} = \hat{S}^*/n_{\hat{S}}$
- 3: **for** $\hat{S} = 1, 1 + \Delta\hat{S}, 1 + 2\Delta\hat{S}, \dots, \hat{S}^*$ **do**
- 4: Compute $\mu(\hat{S}) \leftarrow \mu_0(1 + A \cos(\pi\hat{S}/\hat{\lambda} + \phi))$
- 5: Compute $\beta_0^+ \leftarrow \text{arccot}(-\mu(\hat{S}))$ and $\beta_0^- \leftarrow \text{arccot}(\mu(\hat{S}))$
- 6: Compute $\Delta\beta_0 \leftarrow (\beta_0^+ - \beta_0^-)/n_{\beta_0}$
- 7: **for** $\beta_0 = \beta_0^-, \beta_0^- + \Delta\beta_0, \beta_0^- + 2\Delta\beta_0, \dots, \beta_0^+$ **do**
- 8: Solve for \hat{P}_n as the smallest root of $f(\cdot; \hat{S}, \beta_0)^c$
- 9: Construct $\theta(\cdot; p)$ from (4.16) using \hat{S}, \hat{P}_n , and β_0
- 10: Determine $\hat{w}_0(p)$ and $\hat{F}(p)$ from (4.18), (4.22), (4.16b) and (4.10c)
- 11: Save the points $(\hat{S}, \hat{w}_0(p)), (\hat{S}, \hat{F}(p))$, and $(\hat{w}_0(p), \hat{F}(p))$ as respective members of the equilibrium regions in the \hat{S} - \hat{w}_0 , \hat{S} - \hat{F} , and \hat{w}_0 - \hat{F} spaces
- 12: **end for**
- 13: **end for**
- 14: **Output:** A collection of $n_{\hat{S}} \times n_{\beta_0}$ equilibrium points in each of the \hat{S} - \hat{w}_0 , \hat{S} - \hat{F} , and \hat{w}_0 - \hat{F} spaces

^a The parameter $\hat{S}^* > 1$ specifies the maximum value of \hat{S} among all the computed equilibrium configurations.

^b The parameters $n_{\hat{S}}$ and n_{β_0} , respectively, specify the number of different \hat{S} and β_0 values among the computed equilibrium configurations.

^c defined in (4.27)

Remarks.

1. As can be noted from (4.28), the curve $\gamma_{\text{sp-eq}}$ is parameterized by the total length \hat{S} . The left end of the curve, i.e., the point $(0, 0)$, corresponds to $\hat{S} = 1$ (see Fig. 7(A)). Thus, the value of \hat{S} strictly increases as we travel along the curve starting from the origin.
2. The equilibrium curves from our model for the cases in which $\mu_0 = 0.0$ or 0.6 and $A = 0.0$ or 0.4 are shown in Fig. 8(A). In all cases, as expected, the equilibrium curves predicted by our model asymptote to the one predicted by the EB theory (see equation (5) in Kochiyama et al. (2021)) as the midpoint deflection becomes small.
3. When $A = 0.0$, the most noticeable aspect of the equilibrium curves from our model is that the force initially increases and later decreases with the midpoint deflection. In contrast, in the equilibrium curve predicted by the EB theory (see Fig. 8(A)), the force always increases with the deflection.

4. When $A \neq 0.0$, the equilibrium curves from our model have an undulatory nature. The sawtooth pattern in our model is a consequence of these undulations. The undulations appear to become more pronounced as the values of \hat{S} and \hat{w}_0 increase, starting from when \hat{F} is about to reach its maximum value. As noted from Fig. 2 in the SS experiments, the sawtooth-pattern appears or is pronounced in this very same region.

4.3. Force–displacement curves that will be measured in the simply-supported experiments

In Section 4.2.4, we discussed that only a subset (specifically, the upper envelope) of the spicule's equilibrium configurations is relevant in the loading phase of the SS experiments. In the \hat{w}_0 - \hat{F} space, we termed that upper envelope (4.28) the spicule-equilibrium curve, $\gamma_{\text{sp-eq}}$. The spicule configurations sampled by the experiment have to necessarily lie on $\gamma_{\text{sp-eq}}$. However, not all the configurations in $\gamma_{\text{sp-eq}}$ will be sampled during the loading portion of the SS experiment. This is because the spicule being in equilibrium does not necessarily mean that the MTS's wedge is in one of its equilibrium configurations. The force acting on the spicule's midpoint has to be provided by the wedge's apex (shown marked in Fig. 5(C)). However, that force may not necessarily be balanced by the force acting on the wedge's base due to the MTS's cantilever's deformation.

To be more precise, we analyze the force balance on the wedge of the MTS. We assume that in the SS experiments, the total length \hat{S} evolves in the manner dictated by the function $\hat{S} : [0, \tau^*] \rightarrow [1, \infty)$. As mentioned previously, the experiment will only sample configurations on $\gamma_{\text{sp-eq}}$. At the time instance τ , the measured midpoint deflection will be $\hat{w}_0^+(\hat{S}(\tau))$, i.e., $\hat{w}_0(\tau) = \hat{w}_0^+(\hat{S}(\tau))$, and the measured force acting on the spicule's midpoint will be $\hat{F}^+(\hat{S}(\tau))\hat{f}_2$, i.e., $\hat{F}(\tau) = \hat{F}^+(\hat{S}(\tau))$. This force needs to be provided by the wedge's apex. Therefore, the force acting on the wedge's apex will be $-\hat{F}^+(\hat{S}(\tau))\hat{f}_2$. It follows from (3.1) and (3.3) that the force acting on the wedge's base is $\hat{k}_c(\hat{w}_s(\tau) - \hat{w}_0^+(\hat{S}(\tau)))\hat{f}_2$, where $\hat{w}_s(\cdot)$ prescribes how the stage-displacement evolves with time during the experiment. Therefore, the equilibrium condition for the wedge gives that $\hat{S}(\tau)$ be a root of the function $R(\cdot; \tau) : [1, \infty) \rightarrow \mathbb{R}$,

$$R(\hat{S}; \tau) := \hat{F}_{\text{cant}}(\hat{w}_0^+(\hat{S}); \tau) - \hat{F}^+(\hat{S}), \quad (4.29a)$$

where

$$\hat{F}_{\text{cant}}(\hat{w}_0; \tau) := \hat{k}_c(\hat{w}_s(\tau) - \hat{w}_0). \quad (4.29b)$$

We will be referring to the point $(\hat{w}_0^+(\hat{S}(\tau)), \hat{F}^+(\hat{S}(\tau)))$, where $\hat{S}(\tau)$ is a root of $R(\cdot; \tau)$, an overall-equilibrium configuration at the time instance τ . The overall-equilibrium configurations at the time instance τ can be visualized in the \hat{w}_0 - \hat{F} space (see, e.g., Fig. 8(B)) as the intersection points between $\gamma_{\text{sp-eq}}$ and the graph of $\hat{F}_{\text{cant}}(\cdot; \tau)$.

4.3.1. Evolution postulate and our model's prediction for the measured force–displacement curves

In order to derive our model's prediction for the measured force–displacement curve, we consider a thought experiment in which

$$\hat{w}_s(\tau) = \begin{cases} {}^1\hat{w}_s, & \tau \in (0, \tau_1], \\ {}^2\hat{w}_s, & \tau \in (\tau_1, \tau_2], \\ {}^3\hat{w}_s, & \tau \in (\tau_2, \tau_3]. \end{cases} \quad (4.30)$$

In Fig. 8(B), considering a representative \hat{k}_c , we mark and label the overall-equilibrium configurations at the three different stage displacements ${}^1\hat{w}_s$, ${}^2\hat{w}_s$, and ${}^3\hat{w}_s$. As noted from the figure, there can exist more than one overall-equilibrium configurations at a given stage displacement. At the stage displacement ${}^1\hat{w}_s$, there exists only one overall-equilibrium configuration. We denote the total length in that configuration as ${}^1\hat{S}_1$ and label the configuration as ${}^1\hat{S}_1$ in Fig. 8(B).

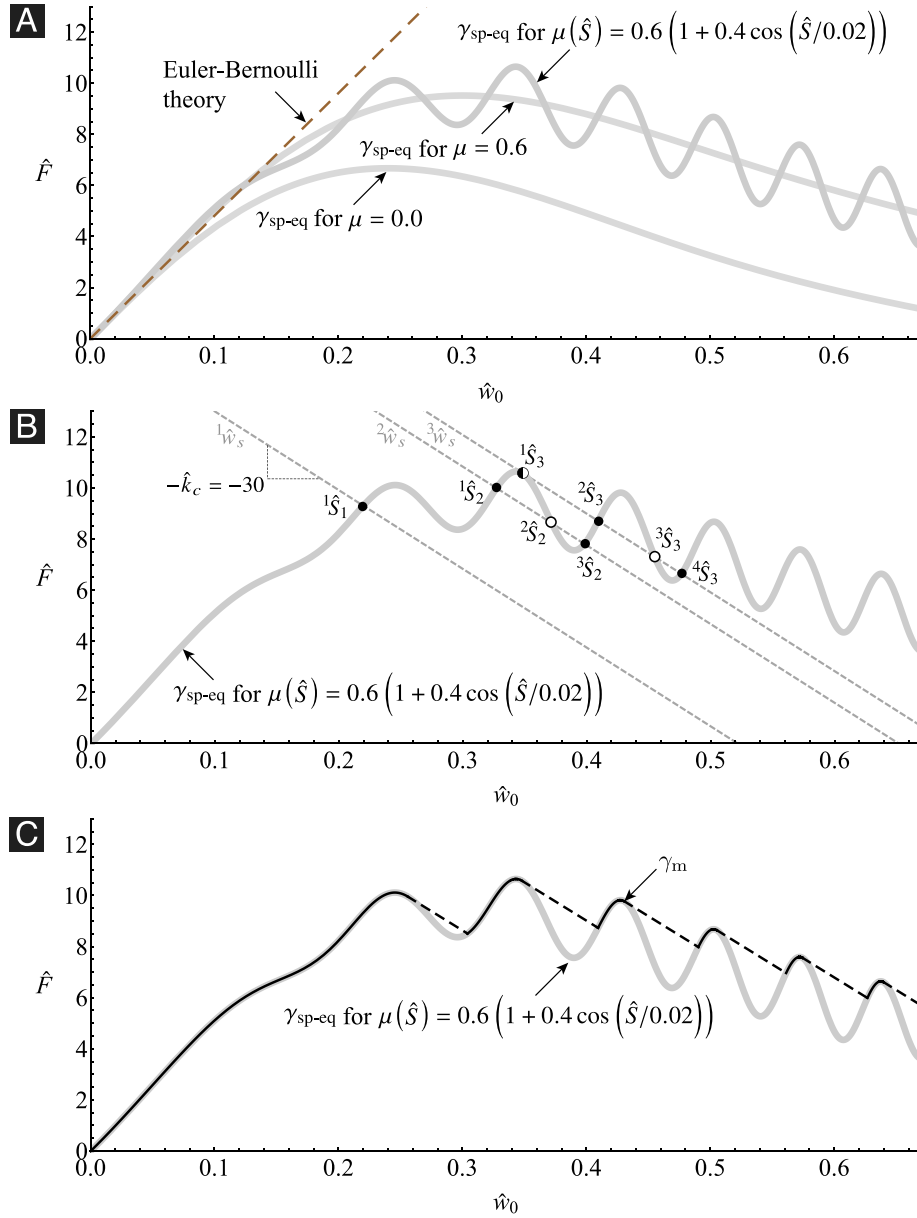


Fig. 8. Equilibrium and measured force–displacement curves. (A) shows the equilibrium curves, γ_{sp-eq} , for the cases $\mu(\hat{S}) = 0.6(1 + 0.4 \cos(\hat{S}/0.02))$, $\mu(\hat{S}) = 0.6$, and $\mu(\hat{S}) = 0.0$, using gray lines. The equilibrium curve predicted by the Euler–Bernoulli theory is also shown for reference, using dashed brown lines. (B) and (C) again show the equilibrium curve corresponding to $\mu(\hat{S}) = 0.6(1 + 0.4 \cos(\hat{S}/0.02))$. They only consider this equilibrium curve and a cantilever stiffness of $\hat{k}_c = 30$ and show the measured curves for two different $\hat{w}_s(\cdot)$. (B) considers the $\hat{w}_s(\cdot)$ given in (4.30) for $^1\hat{w}_s, ^2\hat{w}_s$, and $^3\hat{w}_s$ equal to 0.52, 0.65, and 0.69, respectively. In (B), on the equilibrium curve, we mark the overall-equilibrium configurations at some three time instances that, respectively, belong to the intervals $(0, \tau_1]$, $(\tau_1, \tau_2]$, and $(\tau_2, \tau_3]$, which appear in (4.30). The stable overall-equilibrium configurations are shown as filled circles; the unstable configurations as open circles; and the partially-stable configurations as semi-filled circles. All overall-equilibrium configurations corresponding to the same time instance are connected using a dashed gray line. The three dashed gray lines are the graphs of the function (4.29b) at the three previously mentioned time instances. The graph of the measured curve in this case consists of just the three points that are shown marked as $^1\hat{S}_1, ^1\hat{S}_2$, and $^2\hat{S}_3$. (C) shows the measured curve γ_m for the case in which $\hat{w}_s(\cdot)$ is some continuous, monotonically increasing function of time. The measured curve in this case is the discontinuous curve that is shown using thin black lines. The straight line segments that span the discontinuities of this curve signify the slip instabilities occurring at the trench edges.

However, at $^2\hat{w}_s$, there exist three overall-equilibrium configurations. As before, we label these configurations in Fig. 8(B) using their total lengths, i.e., as $^1\hat{S}_2, ^2\hat{S}_2$, and $^3\hat{S}_2$. At $^1\hat{w}_s$, it is clear that the experiment will measure the total length $^1\hat{S}_1$, i.e., $\hat{S}(\tau) = ^1\hat{S}_1$ for all $\tau \in (0, \tau_1]$. However, at $^2\hat{w}_s$, which one of the three total lengths will the experiment measure? From a theoretical mechanics perspective, the question just posed is the same as the one analyzed in Deng and Kesari (Section 3, 2019b), Kesari and Lew (2011), Deng and Kesari (2021), though the mechanical system investigated in Deng and Kesari (2019b), Kesari and Lew (2011), Deng and Kesari (2021) is different from the one studied in this paper. Following the analysis presented in Deng and Kesari

(2019b), Kesari and Lew (2011), Deng and Kesari (2021), a prerequisite for an overall-equilibrium configuration to be measurable is that it is *stable*. The overall equilibrium state with total length $^j\hat{S}_i$ is stable, iff

$$R'(^j\hat{S}_i; \tau) = -\hat{k}_c \hat{w}_0^{*'}(^j\hat{S}_i) - \hat{F}'(^j\hat{S}_i) < 0. \quad (4.31)$$

Using (4.31), it can be deduced from Fig. 8(B) that $^1\hat{S}_2$ and $^3\hat{S}_2$ are stable, while $^2\hat{S}_2$ is unstable. However, the question still remains as to which of $^1\hat{S}_2$ and $^3\hat{S}_2$ will be measured. To answer this question, as done in Kesari and Lew (2011), we postulate that among the different measurable configurations, the system will evolve into the one that

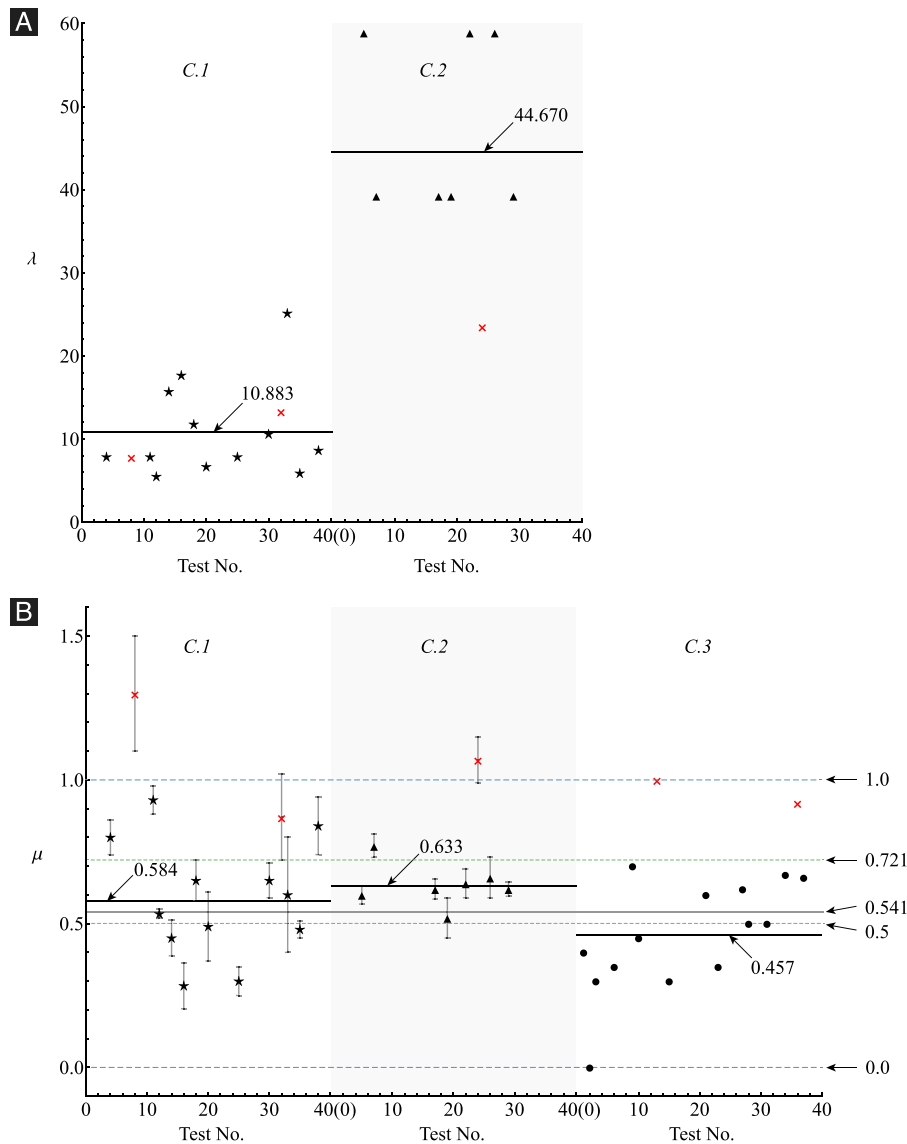


Fig. 9. Distribution of the values we chose for λ and μ_0 to get the predictions from our model for the force–displacement curves to compare favorably with their experimental measurements. Subfigure (A) consists of two plots, which show the chosen values for λ that we arrived at when comparing to curves from C.1 and C.2, respectively. Subfigure (B) consists of three plots, which show the chosen values for μ_0 that we arrived at when comparing to curves from C.1, C.2, and C.3, respectively. All plots belonging to either (A) or (B) share the same y-axis. The x-axis in all plots in (A) and (B) gives the test number, which ranges from 0 to 40. We use black five-pointed star, black up-pointing triangle, and black circle to mark the values we chose when comparing, respectively, to curves from C.1, C.2, and C.3. However, if the curve corresponding to a chosen value also belonged to C.4 then we show that chosen value using a red cross. In each plot a black horizontal line is used to mark the mean of the chosen values in that plot. In computing the means, we excluded a chosen value if the curve that it corresponds to also belonged to C.4. The remainder of the statements in this caption pertain only to (B). The gray horizontal line (labeled as 0.541) that runs across all plots in (B) marks the mean of values we chose for μ_0 when comparing to all curves not from C.4. We mark the maximum (labeled as 0.721) and the minimum (labeled as 0.5) of the measured values for the coefficient of friction between glass and steels that are shown in Table 1. In general, the coefficient of friction is expected to lie between 0 and 1. These two values are shown marked using blue dashed lines. The size of the error bar around each value chosen for μ_0 when comparing to a curve from either C.1 or C.2 is proportional to the value chosen for λ in that comparison. Note that there are no error bars in the plot corresponding to C.3, since when comparing to curves from that category we took $A = 0$ (see Section 5 for details).

is closest to the last measured configuration. In the current case, this evolution postulate implies that the configuration that the system will choose among the measurable configurations will be the one whose total length is closest to the one in the last measured configuration. The last measured configuration in our thought experiment is ${}^1\hat{S}_1$. Therefore, when the stage displacement is ${}^2\hat{w}_s$, amongst ${}^1\hat{S}_2$ and ${}^3\hat{S}_2$, the experiment will measure the one that is closer to ${}^1\hat{S}_1$. It follows from remark 1 in Section 4.2.4 and Fig. 8(B) that ${}^1\hat{S}_1 < {}^1\hat{S}_2 < {}^3\hat{S}_2$. Therefore, at ${}^2\hat{w}_s$, the experiment will measure the configuration ${}^1\hat{S}_2$, i.e., $\hat{S}(\tau) = {}^1\hat{S}_2$ for all $\tau \in (\tau_1, \tau_2]$. When the stage displacement is ${}^3\hat{w}_s$, there are four overall equilibrium configurations. We label those as ${}^j\hat{S}_3$, $j = 1, \dots, 4$, in

Fig. 8(B). Through similar analysis, it can be deduced that the system will measure ${}^2\hat{S}_3$ at ${}^3\hat{w}_s$, implying that $\hat{S}(\tau_3) = {}^2\hat{S}_3$ for all $\tau \in (\tau_2, \tau_3]$.

Now we consider the measured force–displacement curve for arbitrary γ_{sp-eq} , $\hat{w}_s(\cdot)$, and \hat{k}_c . The given $\hat{w}_s(\cdot)$ can be approximated using a function of the form (4.30). For example, we consider a large number of equally spaced time instances in $[0, \tau^*]$, say τ_0, τ_1, τ_2 , etc., and define the value of the approximate- $\hat{w}_s(\cdot)$ for any time instance in $(\tau_i, \tau_{i+1}]$ to be the constant value ${}^{i+1}\hat{w}_s := \hat{w}_s(\tau_{i+1})$. We can construct the evolution of the measured approximate- $\hat{S}(\cdot)$ by carrying out analysis similar to the one presented in the previous paragraph. By increasing the number of time instances, $\hat{S}(\cdot)$ can be approximated to any desired degree.

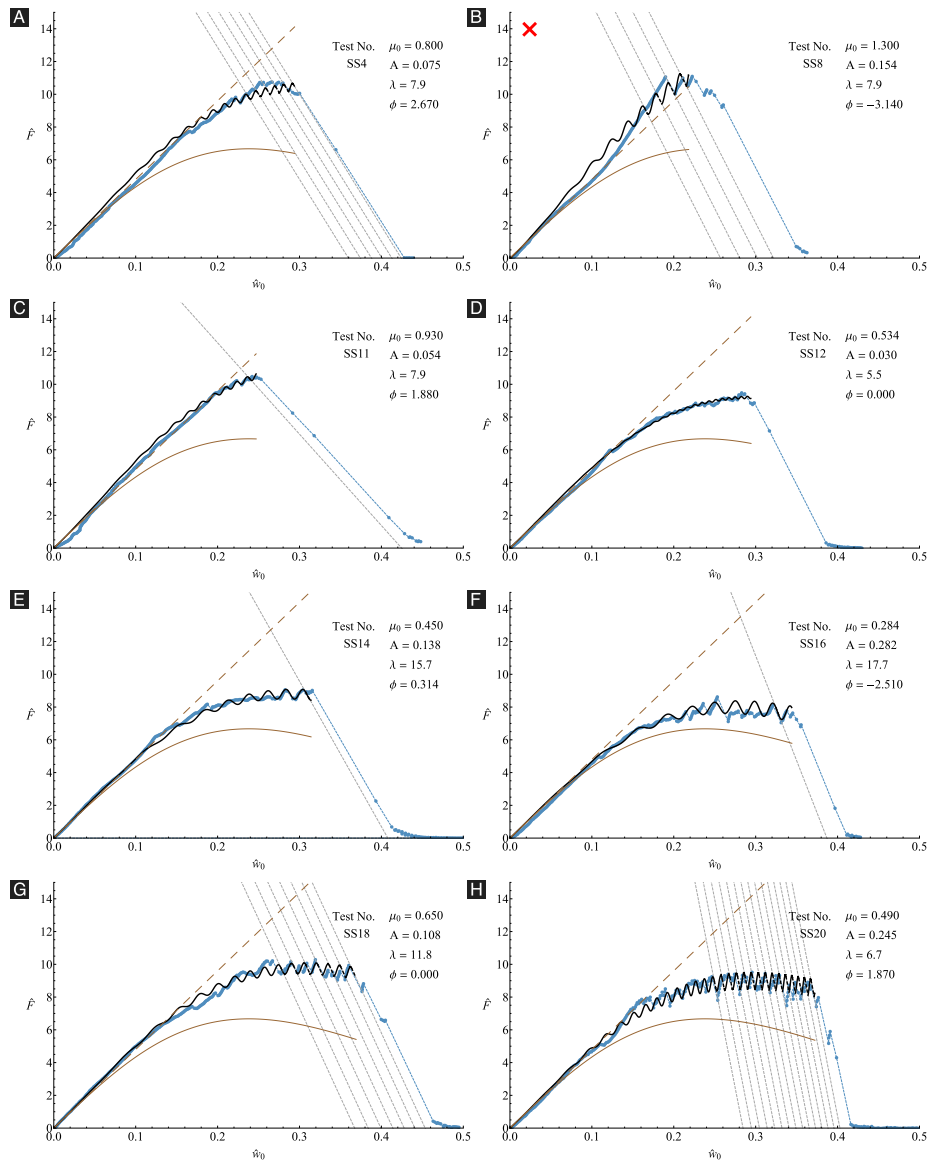


Fig. 10. Comparing measured force–displacement curves from the SS tests belonging to category *C.1* with their theoretical predictions. Each subfigure corresponds to a different test. The subfigures with a red cross mark at their top left corners correspond to tests that also belong to category *C.4*. The following statements apply to each subfigure separately. The experimentally measured force–displacement curve is shown in blue. The prediction from our model for that curve is shown in black. The values we chose for the parameters μ_0 , A , λ , and ϕ in our model for generating that prediction are shown at the top right corner. The predictions from the Euler–Bernoulli theory and from our model for the case $\mu_0 = 0$ are shown using brown-dashed and brown-solid lines, respectively. The gray dashed oblique lines are the graphs of the function (4.29b) at the time instances at which we noted a sudden drop in the measured force. In generating these graphs, in the function (4.29b) we used the \hat{k}_c and $\hat{w}_s(\cdot)$ that we constructed using the experimental details of the test.

After determining the evolution of the measured configuration, i.e., $\hat{S}(\cdot)$, the measured force–displacement curve can be constructed as

$$\gamma_m = \{(\hat{w}_0^+(\hat{S}(\tau)), \hat{F}^+(\hat{S}(\tau))) \mid \tau \in [0, \tau^*]\}. \quad (4.32)$$

We provide a systematic procedure for numerically constructing γ_m in Algorithm 2. In Fig. 8(C), we show a representative γ_m (black) by considering a continuous, monotonically increasing $\hat{w}_s(\tau)$. The corresponding spicule equilibrium curve γ_{sp-eq} (gray) and cantilever stiffness \hat{k}_c are the same as those in Fig. 8(B). As can be seen in (C), the curve γ_m is discontinuous, i.e., it is a union of non-intersecting smooth curves in γ_m using dashed line segments. The dashed line segments physically denote mechanical instabilities. The quantities \hat{w}_0 , \hat{F} , and \hat{S} all change by a finite amount during the occurrence of those instabilities. With its

discontinuities, γ_m , at least qualitatively, captures the sawtooth pattern observed in the SS experiments.

5. Comparing theoretical predictions for the force–displacement curves with their experimental measurements

In Section 4.3.1, we discussed how the force–displacement curves predicted by our model qualitatively capture the sawtooth pattern (see Fig. 8(C)). In this section, we discuss how the predictions from our model for the force–displacement curves compare with their measurements reported in Kochiyama et al. (2021).

Kochiyama et al. (2021) reported measurements of force–displacement curves from 38 SS experiments. We place those curves in the following three categories based on the nature of the sawtooth pattern observed in them.

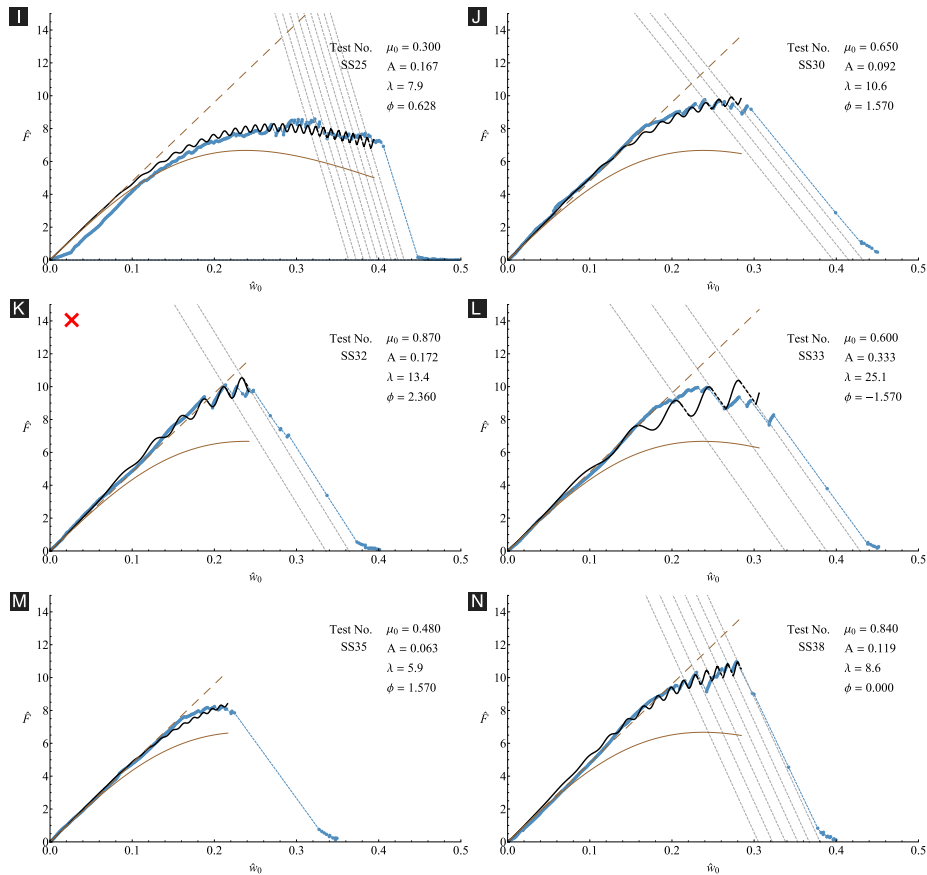


Fig. 10. (continued).

Algorithm 2: Procedure for computing the measured force-displacement curve.

- 1: **Input:** γ_{sp-eq} , $\hat{w}_s(\cdot)$, \hat{k}_c , τ^* , and a natural number n^a
- 2: **Initialization:** $\tau_0 = 0$, $\hat{S}_0 = 1$, $\Delta\tau = \tau^*/n$
- 3: **for** $i = 0, 1, 2, \dots, n$ **do**
- 4: Compute $\tau_{i+1} \leftarrow \tau_i + \Delta\tau$
- 5: Construct $R(\cdot; \tau_{i+1})$ from (4.29) using γ_{sp-eq} , $\hat{w}_s(\cdot)$, and \hat{k}_c
- 6: Solve for the roots of $R(\cdot; \tau_{i+1})$. We denote those roots as ${}^j\hat{S}_{i+1}$, where $j \in \mathcal{J} := \{1, 2, \dots, n_{i+1}\}$
- 7: Set $\hat{S}_{i+1} \leftarrow {}^{k^*}\hat{S}_{i+1}$, where $k^* = \operatorname{argmin}_{k \in \mathcal{K}} |{}^k\hat{S}_{i+1} - \hat{S}_i|$, $\mathcal{K} := \{p \in \mathcal{J} \mid R'({}^p\hat{S}_{i+1}; \tau_{i+1}) < 0\}^b$
- 8: Save $(\hat{w}_0^+(\hat{S}_{i+1}), \hat{F}^+(\hat{S}_{i+1}))$ as a point belonging to the measured force-displacement curve
- 9: **end for**
- 10: **Output:** A collection of n points that belong to the measured force-displacement curve

^a The parameter n specifies the number of computed points on the measured force-displacement curve.

^b $R'(\cdot; \tau)$ is defined in (4.31).

C.1 Curves displaying a clear sawtooth pattern.

C.2 Curves displaying a nominal sawtooth pattern.

C.3 Curves displaying almost no sawtooth pattern.

Category C.1. This category consists of curves from the SS experiments which Kochiyama et al. labeled as SS4, SS8, SS11, SS12, SS14, SS16, SS18, SS20, SS25, SS30, SS32, SS33, SS35, and SS38 (see Fig. 10). There are 14 curves in total in this category.

Category C.2. This category consists of curves from the SS experiments which Kochiyama et al. labeled as SS5, SS7, SS17, SS19, SS22, SS24, SS26, and SS29 (see Fig. 11). There are eight curves in total in this category.

Category C.3. This category consists of curves from the SS experiments which Kochiyama et al. labeled as SS1, SS2, SS3, SS6, SS9, SS10, SS13, SS15, SS21, SS23, SS27, SS28, SS31, SS34, SS36, and SS37 (see Fig. 12). These are 16 curves in total.

We compare our model's predictions with each of the measured curves in Figs. 10, 11 (Category C.2), and 12 (Category C.3). The values of the parameters μ_0 , A , λ , and ϕ were manually adjusted so that our model's predictions matched the measured curves as closely as possible. These manually chosen values are shown alongside each comparison (see top right hand corner of each subfigure in Figs. 10–12). In each of the subfigures of Figs. 10–12, our model's prediction for the measured curve is shown in black (consisting of solid and dashed segments). The measured curve is shown in blue. For reference, we also include the prediction from the EB theory, as well as from our model for the case $\mu_0 = 0$. The prediction from the EB theory (brown dashed) appears as a straight line, while that from our model for the case $\mu_0 = 0$ (brown solid) appears as a section of an upside down parabola.

When comparing our model to the curves from C.1 and C.2, the values of μ_0 , A , λ , and ϕ were adjusted, whereas when comparing to the curves from C.3, only the value of μ_0 was adjusted. We will explain this difference shortly after we discuss the former. The values chosen for ϕ do not have much experimental significance, since they primarily correlate with the position of contacting points between the spicule specimens and the trench edges at the beginning of the experiments. The values of A and λ do have experimental significance, as we expect their values to correlate with the variation in spicules' surface friction.

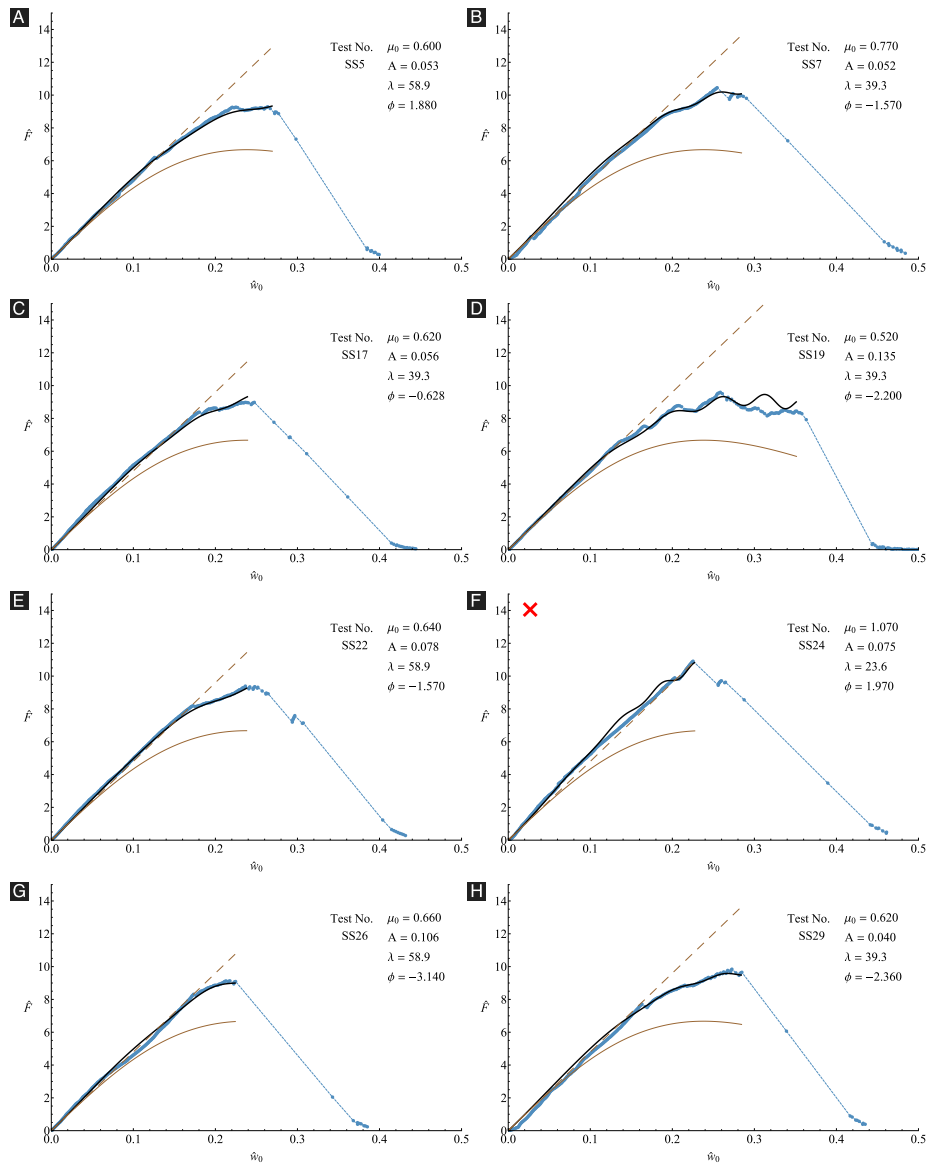


Fig. 11. Comparing measured force–displacement curves from the SS tests belonging to category C.2 with their theoretical predictions. Each subfigure corresponds to a different test. The subfigures with a red cross mark at their top left corners correspond to tests that also belong to category C.4. The statements made in the caption of Fig. 10 that apply to its subfigures individually apply to the subfigures of this figure individually as well.

The mean-range of the values chosen for λ when comparing to curves from C.1 and C.2 are, in the format of mean-(minimum, maximum), 10.883-(5.498, 25.133) and 44.670-(23.562, 58.905), respectively (see Fig. 9(A)). The mean-range of the values chosen for A when comparing to curves from C.1 and C.2 are 0.145-(0.030, 0.333) and 0.074-(0.040, 0.135), respectively. A graphical representation of the distribution of the values chosen for A is shown as error bars in Fig. 9(B).

We would consider the chosen values for A and λ to be reasonable if they were, respectively, close to other estimates of A and λ that were arrived at independently. For ascertaining how reasonable the values chosen for A and λ are, it would be ideal if we could directly measure the variation of the coefficient of friction along the spicules' lengths, perhaps using an Atomic Force Microscope (AFM). Unfortunately, we currently do not have such AFM data available to us (see Section 6 for further discussion).

We considered the possibility of evaluating the values chosen for A and λ using the spicules' SEM images, such as those shown in Fig. 4. Though we believe that the parameter A depends on the spicules' surface topography, we do not currently have an insight into the

mathematical nature of that dependence. Consequently, we are unable to gauge the reasonableness of the values chosen for A from the spicules' SEM images. We are more confident of evaluating λ 's chosen values using the SEM images. We denote the projected thickness of a spicule on an image as z , and define the topography map: $s \mapsto z(s)$. If we calculate the Fourier spectrum of $z(s)$, we expect the dominant angular frequency in that spectrum to be a good estimate for $2\pi/\lambda$. However, we were unable to successfully carry out such an evaluation. The reason behind this can be explained through a rough estimation as follows. As mentioned previously, the means of the values chosen for λ when comparing to the curves from C.1 and C.2 are ≈ 11 and $45 \mu\text{m}$, respectively. In order to evaluate the soundness of these values using the aforementioned Fourier analysis, SEM images with a horizontal field width (HFW) of ideally 10 times the expected wavelength (around $450 \mu\text{m}$) would be needed. The resolution in our SEM images with such HFW would be limited to around $0.29 \mu\text{m}$. Considering that the outer-layer thickness of a spicule is typically $0.4 \mu\text{m}$ (Monn et al., 2015) and assuming that at least 10 pixels are needed on an image for describing the undulation in a spicule's lateral surface, a resolution

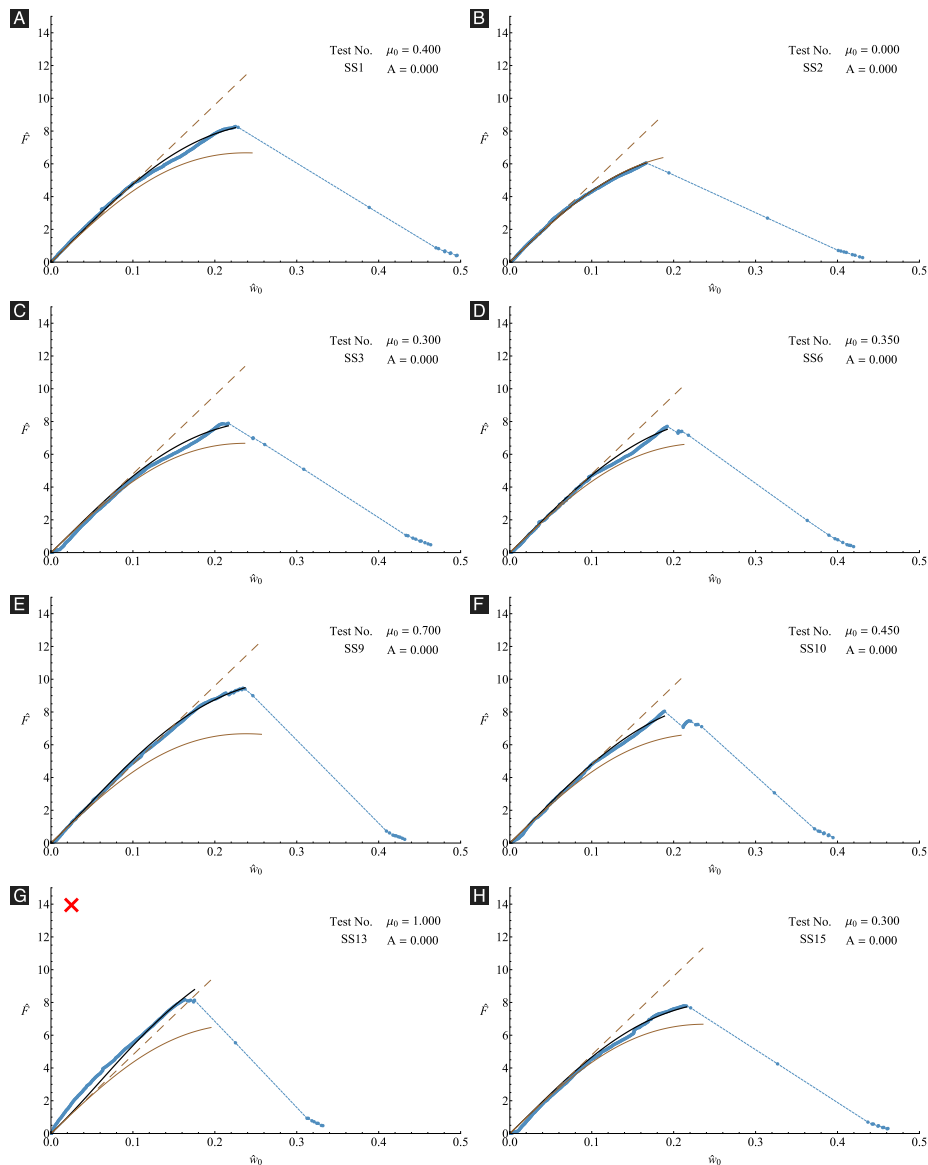


Fig. 12. Comparing measured force–displacement curves from the SS tests belonging to category C.3 with their theoretical predictions. Each subfigure corresponds to a different test. The subfigures with a red cross mark at their top left corners correspond to tests that also belong to category C.4. The statements made in the caption of Fig. 10 that apply to its subfigures individually apply to the subfigures of this figure individually as well.

of ideally 0.04 μm is required. Therefore, the competition between the HFW and the resolution of SEM images prevents us from evaluating the reasonableness of the values chosen for λ from the spicules' SEM images.

When comparing to the curves from category C.3, we only adjusted the value of μ_0 . Our model predicts the lack of any sawtooth pattern when $A = 0$, i.e., when the coefficient of friction is constant along the spicule's length. Since the curves in C.3 displayed almost no sawtooth-pattern, we took $A = 0$ when comparing to the curves from this category. Due to the form of $\mu(\cdot)$ given in (4.25), with $A = 0$, the values of λ and ϕ become irrelevant.

We show the values we chose for μ_0 when comparing to the curves from C.1–C.3 in Fig. 9(B). The mean-range of the values chosen for μ_0 when comparing our model's predictions to the curves from C.1, C.2, and C.3 are 0.656-(0.284, 1.3), 0.688-(0.52, 1.07), and 0.520-(0.0, 1.0), respectively. We consider a final category of curves, C.4, which consists of the curves SS8 and SS32 from C.1, SS24 from C.2, and SS13 and SS36 from C.3. We believe that the curves from C.4 are suspect. Within the context of beam models, the EB theory provides an upper bound

for the force, while our model for the case $\mu_0 = 0$ provides a lower bound. As can be seen from Fig. 13, the forces in the curves from C.4 sometimes exceed the force predicted by the EB theory. We speculate that the spicules in the experiments related to C.4 were unable to slide due to some reason, perhaps due to a protrusion on the spicule's surface getting stuck at the trench's edge. On excluding the curves from C.4, we get the mean-range of the values chosen for μ_0 to be 0.584-(0.284, 0.93), 0.633-(0.52, 0.77), and 0.457-(0.0, 0.7) for C.1, C.2, and C.3, respectively. The mean-range considering all curves except those from C.4 is 0.541-(0.0, 0.93).

As mentioned previously, we were unable to directly characterize the $\mu(\cdot)$ in our experiments. Note that the contact in our experiments is between silica (spicule) and stainless steel (trench edge). Therefore, as an alternative, we compare the values we chose for μ_0 to the values reported in literature for the coefficient of friction between glass and different types of steel, see Table 1. We mark the minimum and the maximum of the values shown in Table 1, which are respectively 0.5 and 0.721, as green dashed lines in Fig. 9(B).

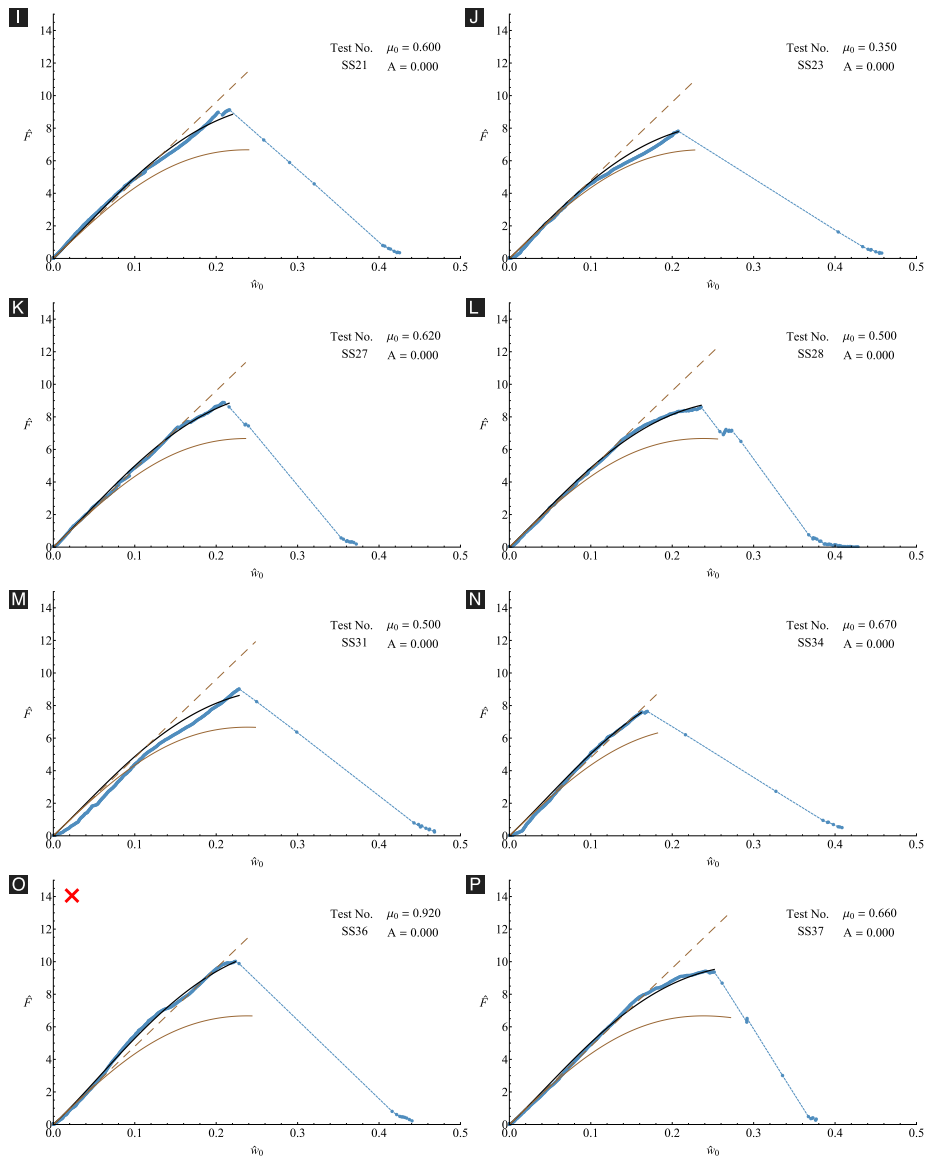


Fig. 12. (continued).

As can be noted from Fig. 9(B), the values we chose for μ_0 are quite reasonable.

6. Concluding remarks

1. As can be noted from Table 1 and Fig. 9(B), the values of μ_0 , which were chosen to match our model's predictions as closely as possible with the measurements of Kochiyama et al. (2021) are quite consistent with the values reported in literature for the coefficient of friction between glass and steel (note that the contact in our experiments is between silica (spicule) and stainless steel (trench edge)). This consistency supports the view that it is valid to use the developed model to interpret Kochiyama et al.'s SS experiments.
2. In order to further gauge the validity of applying the developed model to interpret the SS experiments, it would be ideal if $\mu(\cdot)$, the variation of the coefficient of friction between the spicule and the trench when different cross-sections of the spicule are in contact with the trench, could be measured directly and independently of the SS experiments. In the future, we plan on characterizing $\mu(\cdot)$ using an Atomic Force Microscope (Kesari et al., 2010; Kesari and Lew, 2011; Deng and Kesari, 2019a).

3. Those experiments will provide alternate estimates for A and λ , which can then be, respectively, compared with the chosen values for them. That comparison would allow us to further gauge the validity of applying our model to the SS experiments. It is unlikely that the friction coefficient varies in a sinusoidal fashion along the spicule's length. It is even more unlikely that the coefficient of friction varies in the exact same manner at both the left and the right trench edges during the experiment, as assumed in our model. The goal of assuming that the variation of the coefficient of friction along the spicule's length was symmetric about the spicule's midpoint was to make the problem tractable. However, the decision to model the variation of the coefficient of friction using a single sinusoid was more deliberate. We have compared the predictions from other versions of our model that incorporate more realistic variations for the friction coefficient with the experimental curves. These more realistic variations involved superposition of multiples sinusoids, and consequently involved a larger number of free parameters than the presented single sinusoidal variation, which contains four free parameters, namely μ_0 , A , λ , and ϕ . Unsurprisingly, the predictions from those other versions of our model match the

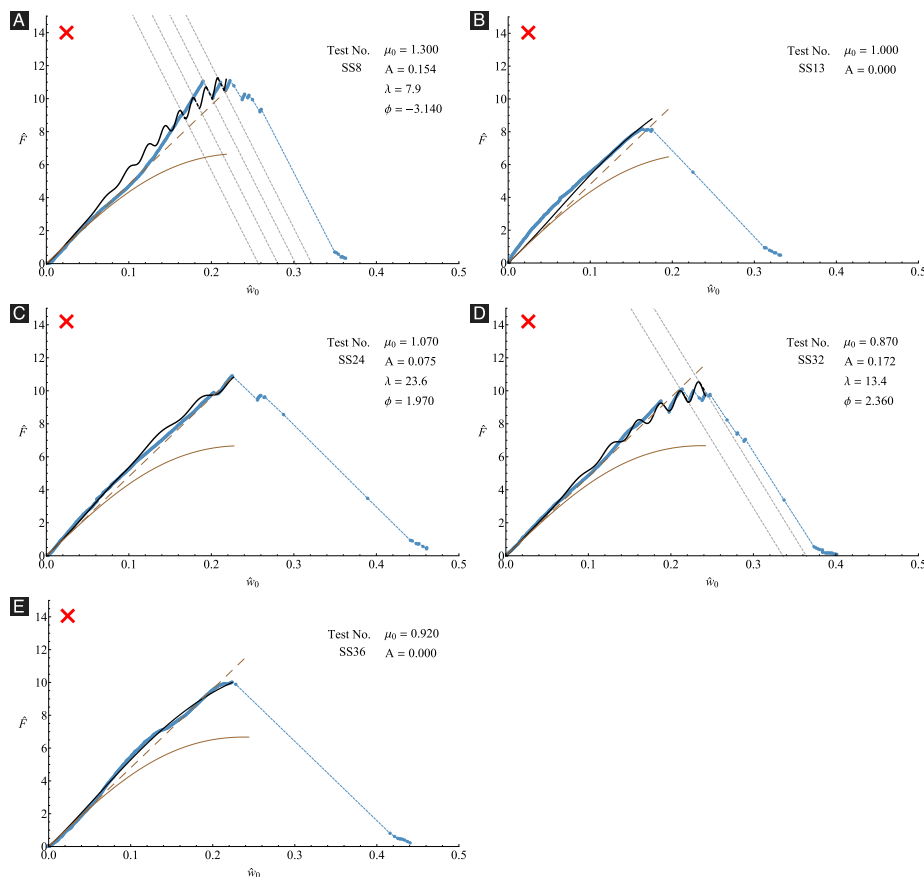


Fig. 13. Comparing measured force–displacement curves from the SS tests belonging to category C.4 with their theoretical predictions. Each subfigure corresponds to a different test. The statements made in the caption of Fig. 10 that apply to its subfigures individually apply to the subfigures of this figure individually as well.

Table 1
Estimates for the coefficient of friction between glass and steel from literature.

Materials	Geometry	Surface condition	Coefficient of friction
Glass–Hard steel (Tomlinson, 1929)	plane–spherical end of a rod (of diameter 2.54 mm)	polished, clean, dry	0.605
Glass–Mild steel (Tomlinson, 1929)	plane–spherical end of a rod (of diameter 2.54 mm)	polished, clean, dry	0.721
Glass–Mild steel (Beare and Bowden, 1935)	plane–sphere (of diameter 5 mm)	polished, clean, dry	0.51–0.61
Glass–Stainless steel (Deulin et al., 2010)	–	polished, in vacuum	0.5
Stainless steel (with silica coating)–Stainless steel (Marsal et al., 2013)	plane–sphere (of diameter 10 mm)	in air	0.7

experimental curves better than those from the presented version of the model. Despite the above fact, we chose to focus this paper on the version based on the single sinusoidal variation, since our primary goal was to present insight into the potential mechanism(s) underlying the sawtooth pattern, rather than to analytically reproduce the measured curves. And among the different versions of our model that we studied, we believe that the one based on the single sinusoidal variation illustrates the sawtooth mechanism captured by our model in the clearest manner.

4. The mechanism underlying the sawtooth patterns in our experiments is similar to the surface topography (roughness) based mechanism put forward for explaining the stick–slip phenomenon (Rabinowicz and Tanner, 1966; Mora and Place, 1994; Berman et al., 1996). The controlling factors in the surface

topography mechanism of stick–slip are the surface’s roughness and the stiffness of the loading system, which are the same as the ones in our model’s mechanism for the sawtooth pattern if we assume that the friction variation in our work is primarily due to the spicule’s surface roughness. One difference in the mechanics of the SS experiments and the stick–slip phenomenon is that in the SS experiments, the spicule is slipping both before and after the occurrence of an instability, while in the stick–slip phenomenon, the specimen is stationary before the occurrence of an instability, and is sliding afterwards.

5. Our preliminary research suggests that there can exist an alternative model for the SS experiments, which is also capable of capturing the sawtooth patterns in the measured force–displacement curves. Interestingly, in that model, it is not required to assume that the coefficient of friction varies along the spicule’s length.

Since we were unable to experimentally ascertain that the coefficient of friction indeed varied along the spicule's length, a model that does not require the assumption of a varying friction coefficient may seem preferable to the one that does. However, this alternative model also contains assumptions that cannot be readily justified through experiments. Furthermore, we were unable to derive any quantitative predictions from that different model for the measured force–displacement curves. For these reasons, we gave preference to the variable friction based model that we presented in this paper.

CRedit authorship contribution statement

Wenqiang Fang: Methodology, Software, Formal analysis, Investigation, Data curation, Writing – original draft, Writing – review & editing. **Sayaka Kochiyama:** Validation, Formal analysis, Investigation, Data curation, Writing – original draft, Writing – review & editing. **Haneesh Kesari:** Conceptualization, Methodology, Software, Resources, Writing – original draft, Writing – review & editing, Supervision, Project administration, Funding acquisition.

Declaration of competing interest

The authors declare that they have no known competing financial interests or personal relationships that could have appeared to influence the work reported in this paper.

Acknowledgment

We thank Michael A. Monn for conducting the mechanical tests. The authors gratefully acknowledge support from the National Science Foundation [Mechanics of Materials and Structures Program, grant number 1562656]; H.K. thanks the American Society of Mechanical Engineers and Brown University for the support provided to him through the Haythornthwaite Research Initiation Grant and the Richard B. Salomon Faculty Research Award, respectively.

References

- Beare, W., Bowden, F.P., 1935. Physical properties of surfaces I-Kinetic friction. *Philos. Trans. R. Soc. Lond. Ser. A Math. Phys. Eng. Sci.* 234 (741), 329–354.
- Beléndez, A., Pascual, C., Méndez, D., Beléndez, T., Neipp, C., 2007. Exact solution for the nonlinear pendulum. *Rev. Brasil. Ensino Física* 29 (4), 645–648.
- Berman, A.D., Ducker, W.A., Israelachvili, J.N., 1996. Origin and characterization of different stick-slip friction mechanisms. *Langmuir* 12 (19), 4559–4563.
- Clegg, W., Kendall, K., Alford, N.M., Button, T., Birchall, J., 1990. A simple way to make tough ceramics. *Nature* 347, 455–457.
- Cook, J., Gordon, J.E., Evans, C.C., Gordon, J.E., Marsh, D.M., Philip, B.F., 1964. A mechanism for the control of crack propagation in all-brittle systems. *Proc. R Soc. Lond. A* 282, 508–520.
- Currey, J.D., 1977. Mechanical properties of mother of pearl in tension. *Proc. R Soc. Lond. [Biol]* 196, 443–463.
- Deng, W., Kesari, H., 2019a. Depth-dependent hysteresis in adhesive elastic contacts at large surface roughness. *Sci. Rep.* 9, 1–12.
- Deng, W., Kesari, H., 2019b. Effect of machine stiffness on interpreting contact force-indentation depth curves in adhesive elastic contact experiments. *J. Mech. Phys. Solids* 131, 404–423.
- Deng, W., Kesari, H., 2021. Angle-independent optimal adhesion in plane peeling of thin elastic films at large surface roughnesses. *J. Mech. Phys. Solids* 148, 104270.
- Deulin, E.A., Mikhailov, V., Panfilov, Y.V., Nevshupa, R., 2010. *Mechanics and Physics of Precise Vacuum Mechanisms*. vol. 91, Springer.
- Euler, L., 1750. De novo genere oscillationum. *Comment. Acad. Sci. Petropol.* 128–149.
- Euler, L., 1952. *Methodus Inveniendi Lineas Curvas Maximi Minimive Proprietate Gaudentes Sive Solutio Problematis Isoperimetrici Latissimo Sensu Accepti*. Vol. 1, Springer Science & Business Media.
- Forsyth, A.R., 1912. *Lectures on the Differential Geometry of Curves and Surfaces*. University Press.
- Goldstein, S., 1938. *Modern Developments in Fluid Dynamics: An Account of Theory and Experiment Relating To Boundary Layers, Turbulent Motion and Wakes*. In: *Modern Developments in Fluid Dynamics*, (V.1), Clarendon Press.
- Jackson, A., Vincent, J.F., Turner, R., 1988. The mechanical design of nacre. *Proc. R Soc. Lond. [Biol]* 234 (1277), 415–440.
- Kesari, H., Doll, J.C., Pruitt, B.L., Cai, W., Lew, A.J., 2010. Role of surface roughness in hysteresis during adhesive elastic contact. *Philos. Mag. Philos. Mag. Lett.* 90 (12), 891–902.
- Kesari, H., Lew, A.J., 2011. Effective macroscopic adhesive contact behavior induced by small surface roughness. *J. Mech. Phys. Solids* 12, 2488–2510.
- Klamkin, M.S., 1962. On the transformation of a class of boundary value problems into initial value problems for ordinary differential equations. *SIAM Rev.* 4 (1), 43–47.
- Kochiyama, S., Fang, W., Monn, M.A., Kesari, H., 2021. Sawtooth patterns in flexural force curves of structural biological materials are not signatures of toughness enhancement. *J. Mech. Behav. Biomed. Mater.* 104362.
- Koester, K.J., Ager, J., Ritchie, R., 2008. The true toughness of human cortical bone measured with realistically short cracks. *Nature Mater.* 7 (8), 672–677.
- Levi, C., Barton, J., Guillemet, C., Le Bras, E., Lehuède, P., 1989. A remarkably strong natural glassy rod: the anchoring spicule of the *Monorhaphis* sponge. *J. Mater. Sci. Lett.* 8, 337–339.
- Marsal, A., Ansart, F., Turq, V., Bonino, J.-P., Sobrino, J.-M., Chen, Y.M., Garcia, J., 2013. Mechanical properties and tribological behavior of a silica or/and alumina coating prepared by sol-gel route on stainless steel. *Surf. Coat. Technol.* 237, 234–240.
- Menig, R., Meyers, M., Meyers, M., Vecchio, K., 2000. Quasi-static and dynamic mechanical response of *Haliotis rufescens* (abalone) shells. *Acta Mater.* 48 (9), 2383–2398.
- Ming-Yuan, H., Hutchinson, J.W., 1989. Crack deflection at an interface between dissimilar elastic materials. *Int. J. Solids Struct.* 25 (9), 1053–1067.
- Monn, M.A., Kesari, H., 2017. Enhanced bending failure strain in biological glass fibers due to internal lamellar architecture. *J. Mech. Behav. Biomed. Mater.* 69–75.
- Monn, M.A., Vijaykumar, K., Kochiyama, S., Kesari, H., 2020. Lamellar architectures in stiff biomaterials may not always be templates for enhancing toughness in composites. *Nature Commun.* 11, 373.
- Monn, M.A., Weaver, J.C., Zhang, T., Aizenberg, J., Kesari, H., 2015. New functional insights into the internal architecture of the laminated anchor spicules of *Euplectella aspergillum*. *Proc. Natl. Acad. Sci.* 112, 4976–4981.
- Mora, P., Place, D., 1994. Simulation of the frictional stick-slip instability. *Pure Appl. Geophys.* 143 (1), 61–87.
- Popov, V.L., 2017. Coulomb's law of friction. In: *Contact Mechanics and Friction*. Springer, pp. 151–172.
- Rabiei, R., Bekah, S., Barthelat, F., 2012. Nacre from mollusk shells: inspiration for high-performance nanocomposites. *Nat. Polym.* 2, 113–149.
- Rabinowicz, E., Tanner, R., 1966. Friction and wear of materials. *J. Appl. Mech.* 33 (2), 479.
- Rahaman, M.M., Fang, W., Fawzi, A.L., Wan, Y., Kesari, H., 2020. An accelerometer-only algorithm for determining the acceleration field of a rigid body, with application in studying the mechanics of mild traumatic brain injury. *J. Mech. Phys. Solids* 104014.
- Sarikaya, M., 1994. An introduction to biomimetics: a structural viewpoint. *Microsc. Res. Tech.* 27 (5), 360–375.
- Sarikaya, M., Fong, H., Sunderland, N., Flinn, B., Mayer, G., Mescher, A., Gaino, E., 2001. Biomimetic model of a sponge-spicular optical fiber – mechanical properties and structure. *J. Mater. Res.* 16, 1420–1428.
- Timoshenko, S., Gere, J.M., 2009. *Theory of Elastic Stability*. Dover Publications, Mineola.
- Tomlinson, G., 1929. CVI. a molecular theory of friction. *Lond. Edinb. Dublin Philos. Mag. J. Sci.* 7 (46), 905–939.
- Weaver, J.C., Aizenberg, J., Fantner, G.E., Kisailus, D., Woesz, A., Allen, P., Fields, K., Porter, M.J., Zok, F.W., Hansma, P.K., Fratzl, P., Morse, D.E., 2007. Hierarchical assembly of the siliceous skeletal lattice of the hexactinellid sponge *Euplectella aspergillum*. *J. Struct. Biol.* 158, 93–106.
- Wegst, U.G., Bai, H., Saiz, E., Tomsia, A.P., Ritchie, R.O., 2015. Bioinspired structural materials. *Nature Mater.* 14, 23–36.
- Whittaker, E.T., 1937. *A Treatise on the Analytical Dynamics of Particles and Rigid Bodies*. CUP Archive.